



THE UNIVERSITY of EDINBURGH  
School of Physics  
and Astronomy

# Astrophysical Uncertainties in Direct Dark Matter Detection

MPhys Project Report

**Freddie Ferguson**

*Submitted for the 40pt MPhys Project course PHYS11016*  
13th March 2019

## Abstract

A systematic uncertainty in the dark matter velocity distribution is explored for the identification of the WIMP mass and WIMP-nucleon cross section from direct detection experiments. This may alter the conclusions that can be drawn from such datasets. A simulation of recoil energy spectra from the LUX experiment, a contemporary dark matter direct detector, is constructed in Fortran. By generating WIMPs from both the Standard Halo Model and a halo-disk-substructure velocity profile, the systematic error on the mass and cross section introduced by uncertainty in the velocity distribution was also analysed, though no value could as yet be reliably specified.

Supervisor: Dr Alex S. Murphy

# Personal statement

The first few weeks of my project were spent familiarising myself with coding in Fortran, which was completely new to me but which I was keen to use in order to maintain consistency with previous research in the field. I also built up my understanding of the theories surrounding dark matter, and how WIMPs can serve as a potential solution. The basic programming proved to be quite time-consuming as I found the logic underpinning the programming language to be significantly different to those that I had used before, and required a much more thorough understanding of the action of the compiler, as well as an understanding of memory allocation and pointers. This proved to be extremely useful later on however, as I was well equipped to interpret the outputs of the simulation and solve the various errors in my code.

The initial aim of my project was to build my own simulation for WIMP particles along the lines of that developed by my professor, Dr Alex Murphy. This simulation aimed to generate datasets modelled on those recorded at the LUX detector, a direct detection experiment searching for dark matter particles. This could then be used for a range of statistical analysis to improve our understanding of the true data.

My first specific task was to generate an  $N$ -body register of particles and assign them velocities randomly-sampled from a Maxwell-Boltzmann distribution in three dimensions. The robust array programming supported by Fortran was immediately beneficial, and the language's highly optimised compiling would later be vital to running the volume of data required efficiently.

The next major task was to perform some simple operations on the particles to replicate the conditions of the real detector, as well as to analyse the output. There are of course a variety of ways to implement the simulation of these particles, and this allowed me to refine my code to ensure that the end result was accurate, stable and easily modified. I also expanded my research surrounding dark matter, broadly covering the status and motivations of research in the field, the growth and relative successes of direct detection methods and the prospects for future research. At this time I became more familiar with the specific aims of my project, in that the initial analysis of the LUX experiment had not included an assessment of uncertainties in the astrophysical parameters, and specifically the velocity distribution. This was something to which I could contribute with the analysis of my simulation.

Once comfortable with the particle arrays, I constructed a procedure to simulate the interactions between incident WIMPs and the LUX detector, and record the resulting kinematics. For the first time this allowed me to compare my simulation of the recoil energies recorded with the real-world data and expectations. It was extremely fulfilling to see the similarities between my generated outputs and that of the detector.

After Christmas, I wrote a module to determine the number of signal events expected to be recorded for an assumed WIMP mass and interaction cross-section, which involved more random sampling and some troubleshooting of Fortran subroutines. With this in place I could now tentatively generate data that modelled that recorded by the LUX experiment. At this

*time I began to analyse the outputs of the simulation, having modified the code to generate outputs for the generated WIMPs and the kinematics of their interactions with the detector.*

*The final major phase of my project involved generating a statistical model to use in order to determine the underlying distribution behind a simulated dataset. A K.S Test was chosen for this, and so I worked to implement an algorithm in my program, with the aid of a similar one used by my supervisor, that would generate the associated p-values for a pair of sampled datasets. This allowed the program to then move towards its ultimate aim; a statistical analysis of the effect of varying the velocity profile on the identification of the WIMP mass and cross section. I updated this to form a two-sample analysis, so that datasets generated under different conditions could be compared. Much of the program was rewritten for this step, so that it could handle a much larger volume of data. This meant devising a number of ways to reduce the computation required, as at first the program would take upwards of two days to run.*

*In fact, I spotted an error in my simulation not long before the deadline where I had averaged the relevant probabilities across the wrong loops; this meant a rerun of much of the results very close to the hand in date. Thankfully I managed to optimise the code so that it could run much quicker (now in around eight hours), and the corrected results were available for this report. Because of this and similar bugs, I was however unable to implement the form factor into the simulation, though the required inputs for this are present in the code, and brief instructions on how to implement this are included in the Appendix.*

*In these final stages I worked to identify the influence of the various inputs to my simulation, and attempted to look for the reasons behind this. It was crucial to build up an understanding of the limitations of my research, and similarly what my results could mean for subsequent real direct detection experiments. Though I was unable to reliably specify a systematic error in this project, I hope that this will provide good grounds for a more thorough investigation of this in the future.*

# Contents

<b>1</b>	<b>Introduction</b>	<b>1</b>
<b>2</b>	<b>Theory</b>	<b>2</b>
2.1	Evidence for Dark Matter . . . . .	2
2.1.1	Galaxy Clusters . . . . .	2
2.1.2	Velocity Dispersions . . . . .	3
2.1.3	Rotation Curves . . . . .	3
2.1.4	State of Evidence . . . . .	4
2.2	The $\Lambda$ CDM Model . . . . .	4
2.3	Known Parameters . . . . .	5
2.3.1	Relic Density . . . . .	6
2.3.2	WIMP-Nucleon Cross Section . . . . .	6
2.3.3	WIMP Mass . . . . .	7
2.3.4	Form Factor . . . . .	7
2.3.5	Dark Matter Velocity Distribution . . . . .	8
2.4	Direct Detection . . . . .	10
2.5	The Lux Detector . . . . .	11
2.6	Kolmogorov-Smirnov Statistics . . . . .	13
<b>3</b>	<b>Methods</b>	<b>14</b>
3.1	Overview . . . . .	14
3.2	Random Number Generation . . . . .	17
3.3	Particle Generation . . . . .	17
3.4	Galilean Transformation . . . . .	19
3.5	Yield . . . . .	20
3.6	Kinematics . . . . .	23
3.7	Detector Flaws . . . . .	26
3.8	Measurement Corrections . . . . .	27
3.9	Statistical Analysis . . . . .	27

<b>4 Results and Discussion</b>	<b>29</b>
4.1 P-Value Analysis . . . . .	29
4.1.1 Standard Halo Model Grid Search . . . . .	29
4.1.2 Necib Model Grid Search . . . . .	32
4.1.3 Quantifying Systematic Errors . . . . .	33
4.1.4 Analysis of Statistical Methods . . . . .	35
4.1.5 Future Improvements . . . . .	36
4.2 Simulation Outputs . . . . .	37
4.2.1 Yield Simulation . . . . .	37
4.2.2 Kinematics . . . . .	39
4.2.3 Limitations . . . . .	40
<b>5 Conclusion</b>	<b>40</b>
<b>Appendices</b>	<b>49</b>
.1 Further Kinematic Outputs . . . . .	49
.2 Xenon Form Factor . . . . .	49
.3 Instructions for implementing Form Factor in Simulation . . . . .	49
.4 Additional Statistical Outputs . . . . .	51

# 1 Introduction

In 2002, Donald Rumsfeld famously characterised knowledge by three categories; that which we know, that which we know we don't know, and that which we don't know we don't know. For a long time, Physics has grappled with both flavours of ignorance. In the present day, the realm of cosmology has begun to establish what exactly it is looking for - which elements of reality have so far lain beyond our grasp. It has been estimated in recent decades that perhaps 95 % of the universe consists of previously unobserved matter [1]. This is a well-supported revelation that places the discipline in a novel state; cosmology has become acutely aware of its deficiency.

Dark matter has emerged as a potential solution to at least some of this deficit. This represents an exciting new area of research, which may have many further implications for physics as a whole. There is speculation that discovery of this new substance may lead to the identification of a supersymmetry between bosons and fermions [2], and may well provide clarity on the unification of Quantum Mechanics and gravity [3]. More immediately, an understanding of the dark matter problem could be the largest advance made in modern cosmology toward a full conception of the large-scale structure of the universe.

The present state of dark matter research is broadly as follows: despite a breadth of evidence for its existence that appears to preclude most other conceivable solutions [4], there has at present not been any confirmed direct detection. The failure to find the proposed particles at a range of energies and cross sections has placed constraints on the form such particles might take [1], and out of such considerations has risen a model of the Weakly-Interacting Massive Particle (WIMP), which is proposed to have a mass on the order of  $10 \text{ GeV}/c^2$  to  $10^3 \text{ GeV}/c^2$ , and to interact primarily via gravity. WIMPs benefit from naturally fitting much of the specification of the anticipated dark matter particles<sup>1</sup>.

First generation direct detection experiments may not have led to a positive discovery, but their results are nonetheless vital for continued research. DAMA/Libra and CoGeNT & Super-CDMS both purported to have found such evidence, but this was not supported by other research groups. It was later found that an underestimation of the background signal from surface events likely led to the excess detection [6]. Over time, events such as this will allow researchers to rule out various discrepancies and refine their methods. There has been clear interest maintained in this area, as the U.S department of Energy and National Science Foundation have announced funding rounds for three new experiments: LZ (succeeding Lux), SuperCDMS-SNOLAB and ADMX-Gen2 [7].

The LUX experiment is a particular focus of this study, which presented its first results in 2013 [8] and provided much foundational analysis for future experiments, such as the upgraded LZ experiment which inherits from both LUX and ZEPLIN [9]. The original analysis applied to its findings did not account for astrophysical uncertainties on their model [8]. The appropriate errors had been previously evaluated by McCabe in 2010 [10], and most have since been incorporated into the appropriate analysis of direct detection.

---

<sup>1</sup>Chief among these is its relic abundance [5], which will be explained in Section 2.3.1.

Nevertheless, it had not previously been considered that the underlying assumptions surrounding the velocity distribution of dark matter could influence their findings. In 2018, Necib et al. conducted a refined analysis and proposed a more sophisticated velocity profile than the incumbent Standard Halo Model [11], derived from evaluation of dark matter simulations and Gaia DR1/DR2 observation of stellar velocity distributions [12]. These two distributions will be used to characterise an uncertainty in the velocity distribution.

This project aims to construct a simulation of the direct detection of dark matter from the LUX experiment, and from this generate pseudo-experimental datasets for a range of parameters. This will firstly provide an analysis of the power of the LUX measurements to identify the WIMP mass and WIMP-nucleon cross section. Secondly, it will assess the effect on this of varying the dark matter velocity distribution. A major problem faced by direct detection is that it is doomed to handle very small sample sizes. It is hoped that this and similar studies will allow future experiments to draw maximum benefit from the limited number of events that can be detected.

## 2 Theory

### 2.1 Evidence for Dark Matter

A brief overview of the motivating evidence for dark matter is provided here. For a more thorough understanding of the state of these and related cases, please see Reference [13].

#### 2.1.1 Galaxy Clusters

The Swiss Astronomer Fritz Zwicky was the first to use the term 'dark matter' in 1933 in relation to observations of the Coma galaxy cluster [14]. His measurements of the cluster mass were achieved by using the Doppler shift of its constituents to find their velocity, and then applying the virial theorem to infer the gravitational force acting on them [15]. This gave a figure much different than that estimated from the luminosity of the system. By comparing the light output to that of the nearby Kapetyn stellar system, the cluster was observed to be roughly four hundred times heavier than its kinematics suggested [16].

This observation came to characterise a class of assertions that galaxy clusters betrayed the presence of previously undetected matter. This could explain much of the kinematics of these systems. In order to do so, this substance would have to make up around 60% of the mass of the structure, and in order to have escaped previous measurement would have to be non-baryonic <sup>2</sup>.

---

<sup>2</sup>Or at least non-baryonic for the most part; some suggest a significant portion of dark matter to be held in brown dwarfs and thus be largely undetected [17], though it seems unlikely this could explain all observed phenomena [18].

### 2.1.2 Velocity Dispersions

A contemporary of Zwicky, Jan Oort, published related research in 1932 that analysed the motion and number density of stars close to the sun and asserted that around 30-50% of the mass implied by their velocities was not visible [19]. This demonstrated that such mass discrepancies existed across a range of magnitudes of observation.

In a return to the Coma cluster, a research time led by S.M. Kent then analysed velocity dispersion profiles on the constituents, and determined a mass-to-blue-light ratio of  $\frac{M}{L} = 181$  [20].

This ratio has been since replicated in a variety of systems, such as the 1974 analysis of spiral galaxies by Ostriker that found a comparable ratio of  $\frac{M}{L} = 200$  [21]. This inferred a mass density for the galaxy that again provided evidence for dark matter. Further studies have since been performed on a range of spiral galaxies in support of this [22], and analysis of the kinematics of dwarf galaxies appears equally illuminating. It is anticipated that low-luminosity systems be dominated by dark matter, and though there are drawbacks to the spectroscopic methods used to quantify their stellar velocities, their analysis supports the presence of dark matter contributing around four-fifths of the mass of the system [23].

### 2.1.3 Rotation Curves

At the galactic scale, analysis of rotation curves has proved instrumental as the clearest evidence for dark matter [24]. Rotation curves are graphs of the circular velocities of stars and gases with respect to the distance from the galactic centre. The theoretical form of these curves is wildly different from that measured, which suggests the existence of further mass in the galaxies than can be conventionally detected [25].

Measured curves, such as that shown in Figure 1, show a roughly flat velocity distribution beyond the galactic core [27]. A simple consideration of Newtonian dynamics reveals that this is far different than the luminous prediction. Consider the velocity of matter in orbit as:

$$v(r) = \sqrt{\frac{GM(r)}{r}} \quad (1)$$

where  $M(r)$  is the total mass of the matter in question,  $G$  is the gravitational constant and  $r$  is the radius of the orbit. This implies that, if  $M(r)$  is given by  $4\pi \int p(r)r^2 dr$ , then it is expected that the mass density  $p(r) \propto \frac{1}{\sqrt{r}}$ .  $v(r)$  is observed to be constant beyond the optical disk, which implies instead that  $p(r) \propto \frac{1}{r^2}$ . This difference in mass presumably arises from the contribution of dark matter, and this provides an estimate of the proportional mass of dark matter to conventional matter. Furthermore, rotation curves for low & high surface luminosity galaxies suggest a universal density profile [28]. Low surface luminosity galaxies are suspected to be everywhere dark matter-dominated [1], and so these are of particular interest in these studies.

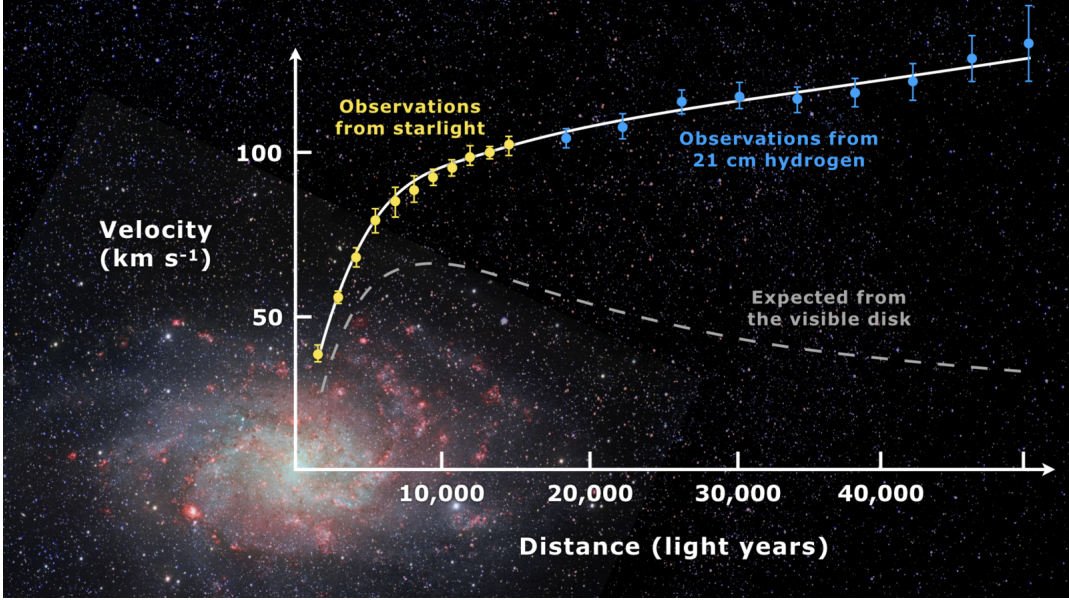


Figure 1. The rotation curve of the Messier 33 galaxy along with prediction [26]

#### 2.1.4 State of Evidence

As such, there is a wealth of evidence at present for some flaw in our understanding of large scale cosmology. Not yet mentioned is the concurrence of the cosmic microwave background and the presence of dark matter<sup>3</sup>. The fact that these observations occur across such a range of scales and systems suggests a universality to the required solution, though there are of course alternatives to the proposed dark matter.

The two most well-supported proposals are a modification to the theory of gravity, and a modification to the cosmological constant of General Relativity. Nevertheless, these both face severe challenges in order to individually replicate the evidence mentioned, amongst other cases [4].

Another quirk of the dark matter problem is that, despite a wealth of evidence for its existence, it is not trivial to extract out clues as to its composition, distribution or behaviour. This is of course largely what this line of research attempts to rectify.

## 2.2 The $\Lambda$ CDM Model

The  $\Lambda$  Cold Dark Matter Model ( $\Lambda$ CDM) provides a framework to describe the structure of the universe in line with the above observations. It is the most favoured contemporary cosmological model. Before 1984 there were many alternate theories proposing hot dark matter, whereby the particle velocities were thought to be relativistic upon decoupling but

---

<sup>3</sup>Dark matter in fact appears to be a natural way to account for the power spectrum of the cosmic microwave background - see [29] and [30] for further discussion.

did not interact electromagnetically. This would mean they would not emit the tell-tale radiation characteristic of relativistic particles. However, a simulation enacted in 1983 by White, Frank & Davis provided strong evidence against this [31].

In place of this, theories positing non-relativistic dark matter labelled ‘cold’ took its place. The ‘ $\Lambda$ ’ in the model describes the presence of Einstein’s cosmological constant to represent dark energy, which will not be the focus of this project. In full, the model can be described by six standard parameters [32], one of which is the dark matter density. The Wilkinson Microwave Anisotropy Probe (WMAP) released findings in 2013 that have tightly defined many of the parameters in this model to fit observations of the Cosmic Microwave Background [32].

Alongside making assertions about the origins of the universe and its basic structure, this model places some initial conditions on the form of dark matter. Previously mentioned is that its velocities are non-relativistic, as the particles would otherwise be expected to emit electromagnetic radiation. The particles are specified to be non-baryonic and collisionless, so that they interact primarily via gravity (and perhaps via the weak interaction) [1]. Lastly they are said to be dissipationless - they cannot radiate photons in order to cool. These constraints have all been implemented to ensure an agreement with the current lack of detection.

A favoured model for these particles is the weakly-interacting massive particle, or WIMP. There are of course a number of alternatives such as MACHOs<sup>4</sup> and so-called WIMPzillas. These will not be analysed in this research.

In a general sense, the term WIMP can be used to describe a number of potential dark matter candidates. In specific usage, it refers to a particle with a mass bounded underneath by the so-called Lee-Weinberg bound at  $2 \text{ GeV}/c^2$  [34] and above by a unitarity bound of 100 TeV [35]. These modest limits have of course since been improved upon, though many assertions are somewhat model-specific. The other key ingredient of a WIMP is that it interacts via the Standard Model weak interaction coupling, which must be heavily suppressed in order to relax constraints on the interaction cross section [36]. The attributes of the WIMP that will be under scrutiny in this project are the WIMP mass and WIMP-nucleon cross section, which form a two-dimensional phase space.

Curiously, the specification for the WIMP coincides with that expected of the particle proposed to underpin a theory of supersymmetry between bosons and fermions, the neutralino. Consult [2] for further discussion of this phenomenon.

## 2.3 Known Parameters

There are a handful of attributes of WIMPs that can be constrained by contemporary observations. It is hoped that over time these limits will be increasingly improved upon to provide a more accurate picture of the nature of dark matter.

---

<sup>4</sup>However the mass that can be attributed to MACHOs has strict limits placed upon it by gravitational lensing surveys of space, as this technique captures objects that emit little or no light [33].

### 2.3.1 Relic Density

An important consideration is the footprint left by dark matter in the early Universe, most clearly visible in the cosmic background radiation [37]. This provided one of the first attributes of dark matter that served to constrain its possible form.

The particles generated in the Big Bang must have existed in thermal equilibrium at some stage, so that forward interactions to new particles balanced with backward interactions to the original one [38]. Once the interaction rate dropped below the universe expansion rate, equilibrium was no longer maintained and the particles decoupled. At this point the particle 'freezes out' and its number density, no longer fluctuating with its interactions, remains constant. The relic density is then the density of the particle at the point of freeze out, which will take the same aggregate value at all subsequent times. The temperature required to provide the observed relic density can be calculated simply by knowing the rate of reaction and the Hubble expansion rate [1].

The relic density forms a useful metric with which to assess potential candidates for dark matter, and has been used effectively to rule out candidates such as Standard Model neutrinos [39]. In the simulation, this will fix the expected mass density of dark matter in the universe at around  $0.3 \text{ GeV/cm}^{-3}$  [8]. Thus, a WIMP with a given mass will have a fixed number density. For a given velocity, this provides a value for the flux of WIMPS through a surface.

### 2.3.2 WIMP-Nucleon Cross Section

The cross section of an interaction in this context is a quantification of the probability that the given interaction will occur, independent of the intensity and focus of the particle beams [40]. It appears reasonable that WIMPs would have some finite coupling with conventional matter. When considering their genesis in the Big Bang, WIMPs would require a cross section of order  $G_F^2 T^2$  in order to achieve freeze-out in the suspected mass range [41]. Underlying this is an assumption that dark matter does indeed undergo annihilation, which is supported by the observed density measurements<sup>5</sup>. Without annihilation, a much greater abundance of WIMPs would be expected. Thus there is implied some interaction of dark matter with baryonic matter.

There has been reasonable theoretical support for finding WIMP interaction cross sections by analogy to the behaviour of comparable known particles [42]. Most attempts at this have been model specific, but a conservative approach is to fix the WIMP-nucleon cross section with regards to its mass in order to replicate the possible rates of interaction observed. Various experiments have proposed upper bounds on this value [43] [44], though the lower bound is harder to probe without progressively more sensitive instruments [45].

The cross section for WIMP-nucleon scattering combines two components; the cross section at zero momentum transfer, as well as a contribution from the nuclear form factor. The form factor will be discussed fully in Section 2.3.4.

---

<sup>5</sup>Crossing symmetry suggests that the amplitudes of annihilation and baryonic interaction are related for dark matter particles. [?]

To arrive at an estimate of the WIMP-nucleon cross section, the coupling with quarks and gluons can be considered individually, and then the matrix elements of quark and gluon operators in a nucleon state used [46]. The nuclear form factor serves to incorporate the various wave functions and the subsequent effect on the cross-section [47].

The range within which WIMP interaction cross sections are considered in the accompanying experiments is generally on the order of  $10^{-45}$  to  $10^{-43} \text{ cm}^2$ . This has been selected in order to mirror the cross sections implied from contemporary experiments.

### 2.3.3 WIMP Mass

Previous attempts at the measurement of WIMPs have been successful in bounding the possible mass of these particles where they have otherwise failed to detect them. These constraints build on the aforementioned Lee-Weinberg Limit and the Unitarity Limit mentioned previously.

Since the late-time annihilation of WIMPs would leave a trace in the cosmic microwave background, and these are not observed, then an upper limit can be placed on the annihilation cross section based on the relic density, in order to constrain its occurrence to the early universe [48].

A refined lower mass limit can then be calculated by relating the relic density bound on WIMPs to the annihilation cross section necessary to have reached equilibrium at this value [48]. For these relic particles, their abundance depends only on their mass and their thermally-averaged annihilation cross section [38]. The failure to observe traces of late-time WIMP annihilation places an upper bound on this cross section, which in turn leads to a lower bound on the WIMP mass via an energy argument. This amounts to  $50f \text{ GeV}/c^2$ <sup>6</sup>, where  $f \leq 1$  and f is an electromagnetic efficiency factor [48]. Indeed, as of 2018 a more conservative but model-independent lower bound was set using similar logic of  $m_{min} \geq 20 \text{ GeV}/c^2$  [49].

Speculatively there is a lot of scope for an increasingly heavy WIMP, with extensions towards so-called 'wimpzillas'. Nevertheless it is largely expected that these particles will at most have mass on the scale of  $10^3 \text{ GeV}/c^2$ , as this is the most easy conception to incorporate into the  $\Lambda\text{CDM}$  Model [50].

### 2.3.4 Form Factor

Due to the scale of the particles involved, the scattering of WIMPs from nuclei is such that the de Broglie wavelength must be considered. The wave-like properties of the incident particle in this case leads to an interference pattern in the subsequent scattering profile [51]. It is later shown that the angle of recoil holds a direct relationship to the energy imparted

---

<sup>6</sup>This is applicable if the WIMP is its own anti-particle; if not, this is a factor of two larger [48].

to the nucleus, and so the form factor leads to a modulation of the energy spectrum. In practice, a WIMP of a given mass will experience destructive interference at certain energies, and no interactions will be expected to be observed. In Figure 2, a characteristic graph of the structure (form) factor of an isotope of Xenon is shown. This is the element of choice for the Lux and LZ experiments).

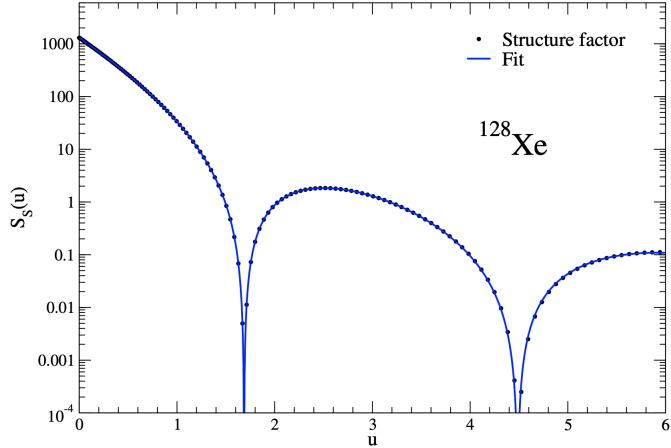


Figure 2. The Structure (Form) Factor for  $^{128}\text{Xe}$  with a fit provided in blue, courtesy of [52].

Evidently Xenon has a relatively low cross section in the relevant energy range  $\sim 20 \text{ keV}$ , but makes up for this somewhat as its large atomic mass provides strong spin-independent coupling, as discussed in Section 2.4. Nonetheless, a variety of elements have been used in direct detection with success.

### 2.3.5 Dark Matter Velocity Distribution

Consider briefly the rotation curves recorded for galaxies such as Messier-33 [27] (see Figure 1). It is clear that the distribution of dark matter in a system ought to lead to a flat rotation curve, as observed. The simplest means to achieve this is to assume an isotropic, isothermal state for the dark matter, which takes the Maxwell-Boltzmann distribution for its velocities:

$$f(v) \propto v^2 \exp\left(-\frac{v^2}{2\sigma^2}\right) \quad (2)$$

This broadly makes up the assumptions of the Standard Halo Model (SHM), which is sufficient to describe observation up to some degree of accuracy. This has proved a useful initial hypothesis for the local distribution of dark matter. Support for this theory came from a 2016 simulation by Navarro et al. that suggested the dark matter composition to be roughly isothermal [53].

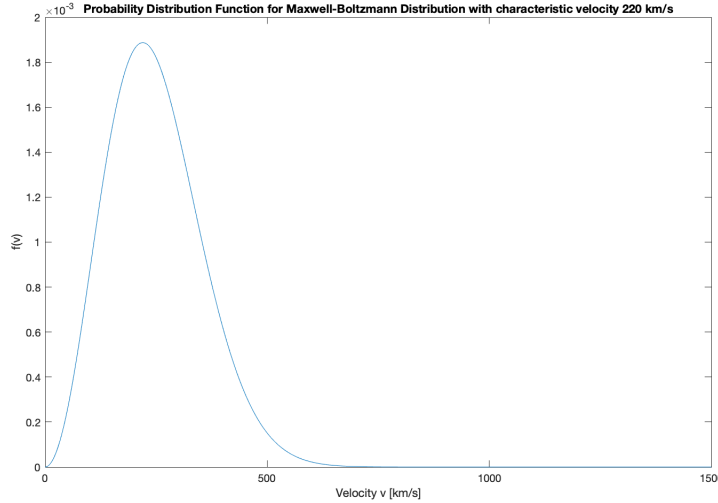


Figure 3. The form of the characteristic normalised Maxwell-Boltzmann velocity distribution

Of course there has been plenty of evidence that the Standard Halo Model is limited in its representation of real dark matter [54] [55] [56], in particular when considering higher velocities. More sophisticated models have since incorporated additional components alongside the halo, often consisting of a thin disk and substructure [57].

Simulations performed by Necib et al. [11] demonstrated in 2018 that the distribution of luminous matter in a galaxy traces the form of the distribution of the associated dark matter. This allows observation of the baryonic matter in a galaxy or cluster to form a crucial window into the underlying dark matter distribution.

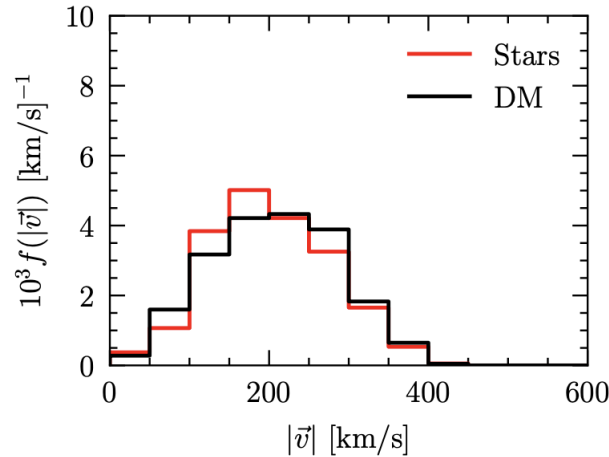


Figure 4. A comparison of the velocity distributions of stars accreted from an old satellite, redshift 4, and its surrounding dark matter. This illustrates the relationship between the velocity distributions of the luminous and dark matter constituents of a system discovered by Necib et al. Figure provided by [58]

Similarly, this revelation indicates that the dark matter distribution depends on the formative history of the luminous matter in the system [11]. This research team provided an alternative velocity profile based on this observation, which is an example of the halo-disk-substructure model mentioned. As such, the halo forms from the oldest accreted dark matter in a system, whilst newer additions, from younger stars and gas, are not yet fully incorporated and so take the form of a thin disk and substructure [11], which will inherit dynamics from its accretion history. Observations from Gaia have been instrumental in providing grounds for these assertions [12]. The more sophisticated velocity distribution arising from this analysis, shown in Figure 5, will be referred to as the Necib model in this paper for brevity.

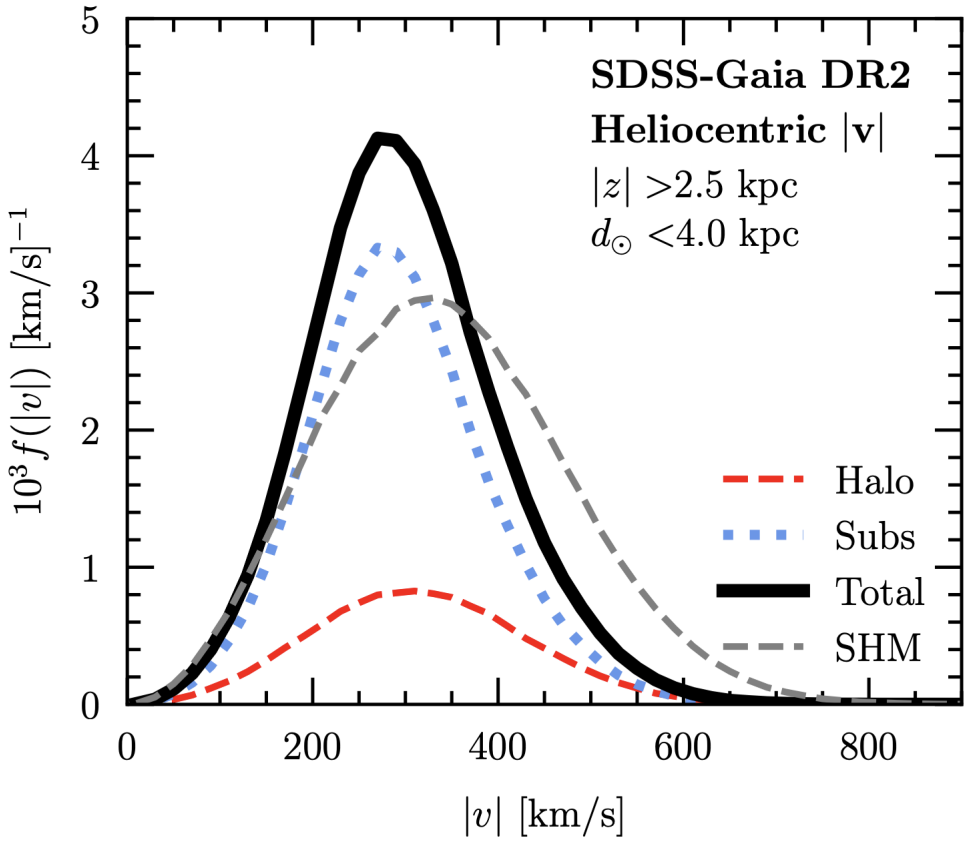


Figure 5. The superposition of a proposed DM halo, substructure and disk lead to a new model for the WIMP velocity distribution. Figure provided by [11].

## 2.4 Direct Detection

There have been a variety of methods attempted in order to observe dark matter particles. This research relies on direct detection such as that used at the LUX and XENON experiments, though many observations alternatively focus on detecting the products of dark matter annihilations [59], which constitute indirect detection. Similarly, there is speculation that dark matter particles ought to be light enough to be produced in colliders such as the LHC, though this line of inquiry has, as yet, born no fruits [60].

Direct detection relies on observing the interaction of dark matter with some detector structure. Naturally this method requires the specification of some broad model for the dark matter, in order to select the range of interactions to look for and observe. Consider that the method of measurement you would wish to use would differ dramatically depending on whether you expected to find a cannon ball or a shuttlecock!

Naturally this process relies on the assertion that WIMPs, of some permissible mass and cross section, are the correct model with which to interpret dark matter. If WIMPs are indeed the culprit behind the large-scale phenomena we observe, then a large flux of them will pass through the Earth at any one time. If at least some of these interact with baryonic matter, it ought to be possible to detect the recoil energy of nuclei interacting with these WIMPs [61].

There are two possible forms of interaction proposed: the first, spin-independent, presumes that the interaction couples to the mass of the target particle. The second, spin-dependent, assumes a coupling to the spin of the nucleus of the target [62]. In general, spin-independent scattering will likely be easier to detect as in the spin-dependent case pairs of spins cancel their contributions.

In such scattering events, the differential energy spectrum of the recoils takes the form:

$$\frac{dR}{dE_R} = \frac{R_0}{E_0 r} \exp\left(\frac{-E_R}{E_0 r}\right) \quad (3)$$

with  $r$  being the kinematic factor  $r = \frac{4M_\chi M_t}{(M_\chi + M_t)^2}$ ,  $E_R$  being the recoil energy and  $E_0$  the most probable kinetic energy of incident dark matter particles, mass  $M_\chi$  [46].  $R$  and  $R_0$  represent the rate of interaction and a proportionality constant respectively. In later sections the modifications necessary to apply this to a real detector are outlined.

It is important to note that, as of this report, there has not been confirmation of a successful direct detection of dark matter [9]. As such, contemporary experiments generate limit plots that bound the possible event rate.

## 2.5 The Lux Detector

The simulation used is modelled on the setup for the Large Underground Xenon Detector (LUX) experiment. This is an example of a noble gas detector, though there are other types, such as the cryogenic detectors used at CDMS II [63].

Noble gas detectors work by detecting the products of interactions between incident radiation & matter and the target, usually Xenon or Argon, which must be cooled to its liquid phase. An array of photomultipliers is placed on the upper and lower surface of the liquid, and two signals can then be recorded. Particle interactions in the target trigger scintillation, which release liberated electrons. As shown above, an applied electric field leads these to

collect on the upper surface of the detector, where they enter the gas phase of the Xenon. This causes electroluminescence, where a second light signal is generated proportional to the electric charge [64].

There are two main subcategories of noble gas detectors dependent on the analysis of their targets: single phase detectors, and double phase time projection chambers. The latter is that used for LUX [8], and benefits from better vertex reconstruction (to locate coordinates where interactions occur) and thus more accurate event discrimination [65]. In these detectors, the scintillation light and ionization charge are both measured for a given event.

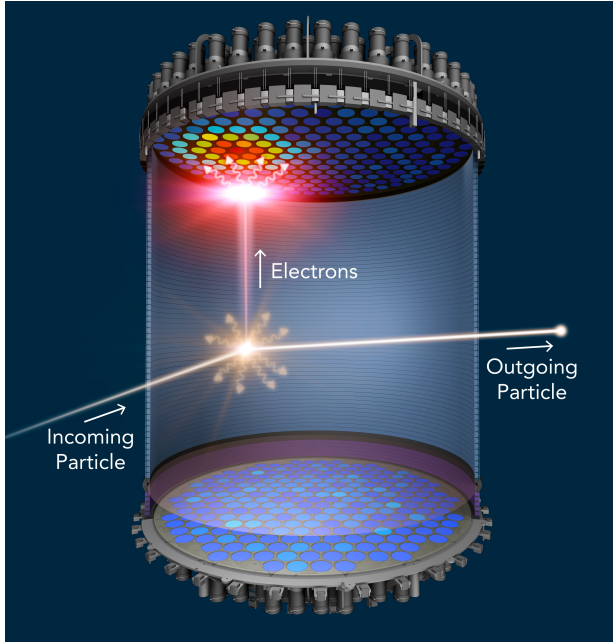


Figure 6. A diagram of the LUX detector, provided by [66]. Note the layers of photomultiplier tubes on the top and bottom of the liquid Xenon interior

The LUX detector is an effective example of such a detector, consisting of 370kg of liquid Xenon housed at the Sanford Underground Research Facility in Lead, South Dakota [8].

The desired signal for this detector can be distinguished from background by considering four parameters: the radius, depth into the detector, intensity of light signal and charge from each event. In order to reduce the prevalence of background radiation, these detectors are typically placed underground and encased in shielding. A  $7.6m \times 6.1m$  water tank is placed around the LUX detector, itself located 1.5km below the surface [42]. There are generally three sources of background radiation. The first, external backgrounds arising from cosmic rays and similar, can be minimised effectively by the isolation of the detector mentioned above. Consider that in all likelihood, if such radiation has reached the detector, it is very likely to simply pass straight through without reacting. The steps taken have been shown to reduce this source of background by a factor on the order of  $10^{-6}$  [67]. The second main source is internal backgrounds arising from the detector instruments <sup>7</sup>, and the third is interaction

---

<sup>7</sup>These can arise from interactions in the photomultiplier tubes, for instance.

of the liquid Xenon. These are more difficult to mitigate. These are largely excluded by consideration of the ratio of the scintillation light (S1) to charge (S2) which can distinguish between nucleon and electron recoils [8]. Measuring the time difference between the signals on the upper and lower surface allows the depth of the interaction to be calculated, and the location of the charge on the surface provides an x-y location for the event [67]. The rate of background interactions of the Xenon can be modelled for every point in its volume, and so knowing the location of the collision aids in accurately discriminating the signal above the background. The detector also benefits from 'fiducialisation', whereby only the centremost region of the target is considered for data acquisition, so that the surrounding zone acts as added shielding. Most of the background events are found to occur near the surfaces [42], so this further serves to improve accuracy.

Though LUX has been unable to conclusively detect a WIMP directly, the experiment has been successful in placing confidence intervals on the spin-independent WIMP-nucleon cross section. At the 90% confidence interval, the upper limit on the number of expected signal events across a range of potential masses was between 2.4 and 5.3 [8].

## 2.6 Kolmogorov-Smirnov Statistics

It is necessary in the subsequent simulation to place a degree of belief on whether a signal of a limited number of readings corresponds to some underlying distribution. The method chosen to do this utilises the Two-Sample Unbinned Kolmogorov-Smirnov Test (K. S. Test). This is an instance of a non-parametric test, and so does not depend on the underlying distribution [68]. This explanation follows the logic of Massey in his 1951 paper on the subject [69] as well as Marsaglia in the following article [70], which can be consulted for further insight.

The test proceeds as follows. The aim is to discern whether two samples are generated from the same distribution. The null hypothesis  $H_0$  for this case will be that the collected samples arise from the same distribution, whilst the alternate hypothesis  $H_1$  is that they do not.

The first step is to construct the empirical distribution functions for the two samples, defined as:

$$F^{obs}(x) = \frac{\text{number of observations below } x}{\text{number of observations}} \quad (4)$$

So that  $F^{obs}(x)$  gives the proportion of datapoints below  $x$ . The K.S statistic quantifies the maximum distance between the two cumulative functions, and is defined as:

$$D_n = \max_x | F_1^{obs}(x) - F_2^{obs}(x) | \quad (5)$$

This statistic is calculated at all points along the distributions, and the maximum value taken. This maximum value is the D-statistic, and from this the p-value can be calculated.

In this analysis it is not known which of the two samples will be above or below the other, and so a two-tailed test is used. The calculation of a p-value from this maximum distance  $D_n$  proceeds as follows. The p-value for some value  $D_n$  between two samples m,n represents the following probability:

$$p = P(D_{m,n} \geq D_{obs} | H_0) \quad (6)$$

Where  $D_{m,n}$  is the maximum value between the distributions m and n,  $D_{obs}$  is the characteristic distance between identical samples, and  $H_0$  here means that the probability is calculated given that the two do indeed derive from the same distribution. In other words, p represents the probability that the true value of the K.S D-statistic is greater than or equal to that observed. In his 1939 article [71], Smirnov demonstrated that:

$$\lim_{n,m \rightarrow \infty} P(D_{obs} \geq \sqrt{\frac{mn}{m+n}} D_{m,n}) = L(D_{obs}) \quad (7)$$

where:

$$L(D_{obs}) = 1 - 2\sum_i^{\infty} (-1)^{i-1} e^{2i^2 D_{obs}^2}$$

Clearly it is very complex to deal directly with  $D_{m,n}$ , and so a variety of methods are used to devise good approximations for the p value required.

For two identical samples, the p-value would be 1.0, as there would be no distance between the two c.d.fs at any point. For two different samples drawn from the same underlying distribution, a uniform range of p-values from 0 to 1 would be expected, which would take a mean of 0.5. Increasingly small p-values indicate a decreasing degree of belief that the two are drawn from the same distribution.

There are alternative statistical tests that can be performed for the same purpose, most notably the Pearson  $\chi^2$  test. The K. S. Test however holds some advantages, chief among which being its validity when analysing small sample sizes [72].

## 3 Methods

### 3.1 Overview

The primary product of this research is of course the simulation constructed, which sets out to generate pseudo-experimental datasets for the LUX direct detector. This follows the structure shown in Figure 7. Below is an attempt to explain each component of the program. The full code used is stored at <https://github.com/ferguso11/darkmatter>, with more outputs provided.

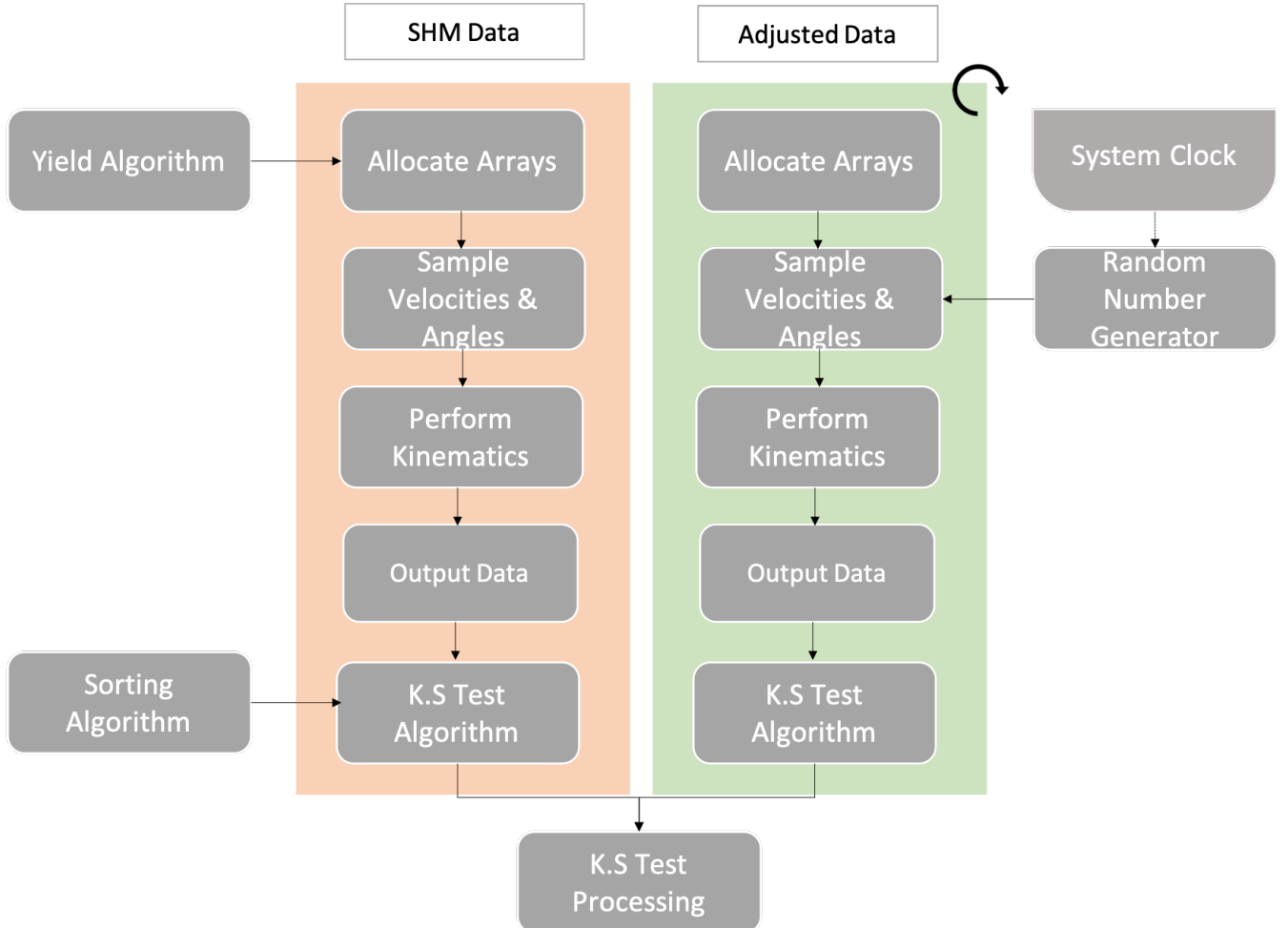


Figure 7. A visualisation of the various elements of the simulation. The simulation in orange (the target) is completed once at the start of the program and stored. The simulation in green (the sample) is rerun for each iteration and compared to the target. The modules on either side apply to both columns equally but are shown on only one side for ease of visualisation.

The simulation stores two recoil spectra at any one time. The first is a large dataset of 10,000 events (shown in orange on Figure 7) drawn from the Standard Halo Model, with some choice of WIMP mass and WIMP-nucleon cross section. The two choices for this project were for  $m_W = 100 \text{ GeV}/c^2$ ,  $\sigma = 9 \times 10^{-45} \text{ cm}^2$ ; and secondly for  $m_W = 60 \text{ GeV}/c^2$ ,  $\sigma = 4 \times 10^{-44} \text{ cm}^2$ , though a variety of choices for this would be equally valid. By testing the analysis with two separate target datasets, this helps to identify the patterns common for any assumed WIMP model. This dataset will be referred to throughout as the ‘target’. The simulation then generates data corresponding to a WIMP mass and WIMP-nucleon cross section drawn from a point in the two-dimensional phase space defined by these parameters. The number of events simulated depends on the output of the yield algorithm for these values. This will be referred to as the ‘sample’ dataset.

The analysis then aims to achieve two main goals: the first is to identify the power of a LUX measurement to identify samples that correspond to some mass and cross section. In other words, how accurately can the mass and cross section be specified based on this reading? This will take the form of finding a region in a two-dimensional WIMP mass/WIMP-nucleon cross section phase space within which the samples are identified as matching the target dataset. The width of this region along the mass axis will represent the mass resolution of the statistical analysis, whilst the width along the cross section axis will similarly reflect the cross section resolution.

For this purpose, a K.S Test is performed between a sample at each point in the phase space and the target, and a mean p-value allocated to them. The region is defined to capture all the space within which the p-value is greater than 0.155, corresponding to one sigma, though this threshold is varied in some of the analysis. This is taken to signify that the sample was indeed identified as matching the target.

The second aim is to investigate how this region changes when the sample is drawn from a Halo/Disk/Substructure velocity profile such as laid out by Necib et al. [11]. This would model the case where the analysis assumes the Standard Halo Model (SHM), but the WIMPs in fact arise from the Necib model. In other words, if we have mistakenly assumed the SHM when the Necib model is in fact valid, what is the subsequent effect on our ability to correctly identify the WIMP from a given measurement? A significant shift in this region could come to characterise a systematic error in the WIMP mass/cross section based on an uncertainty in the velocity distribution.

This second stage involves a repeat of the above, but with the samples now drawn from an approximation of the Necib model distribution [11]. A shift in the p-value distribution indicates the power of an uncertainty in the velocity profile to introduce a systematic error in the identification of the WIMP mass and cross section.

The following sections now explain how each stage of the simulation served to deliver on the above aims.

## 3.2 Random Number Generation

Before proceeding with the main bulk of the simulation, it is important to clarify the pseudo-random number generation used throughout. In cases where a large bulk of random numbers need be generated one after another, the native function ‘rand(0)’ provided by Fortran is used. This pulls values from a stored list of pseudo-random values from a 256-bit state array [73]. The simulation simply selects the numbers consecutively from this list, and so any two runs of the simulation will return the same list of n random variables. However, since the number of values required in these instances is so large in most instances, and since the order in which the particles is processed does not influence the results, then it is taken that this will not significantly bias the outputs of the simulation.

In some instances however it is necessary to generate a single uniform random number, and the above method is ineffective. In order to provide a level of unpredictability, and if nothing else in order to aid in analysing the simulation, a new random number generator is used. This takes advantage of the native system clock to vary the seed of the random number as follows: the program first records the time provided by the system clock, then takes the remainder (also referred to as the modulus) of this number divided by some factor f. This value was varied to optimise the variety in the seed found. This remainder was then passed to the conventional random number generator as a seed, and the random number stored in this location is passed to the program. More explanation of this is provided in Section 4.2.1.

## 3.3 Particle Generation

The first main objective of this research is to generate an array of WIMP particles sampled from the relevant velocity distributions. These can then be manipulated at later stages. As the number of particles to be simulated will need to be varied throughout, the particles are stored in dynamic arrays. These maintain an efficient use of memory, so that extra space is not allocated for shorter particle lists and so that there is no risk of any empty values influencing later analysis.

The particles need only have a velocity vector assigned to them at this stage. To represent the Standard Halo Model, a Maxwell-Boltzmann distribution is constructed as shown, with parameter  $\sigma = 220 \text{ km s}^{-1}$ <sup>8</sup> and the normalisation N set in order to fix the area under the curve to 1. Note that this distribution of velocities is intended to be valid in reference to the frame of the galaxy.

$$f(v) = N v^2 \exp\left(-\frac{v^2}{2\sigma^2}\right) \quad (8)$$

The other main velocity distribution of interest in this project is that arising from the Necib model. A simple way to approximate this new profile is to construct a Maxwell-Boltzmann

---

<sup>8</sup>This value is chosen to comply with the anticipated mean velocity [74].

distribution, but reassign the sun's velocity from  $220 \text{ km/s}$  to  $190 \text{ km/s}$  when performing the subsequent transformations. Figure 8 below shows the effectiveness of this approximation in the simulation in reproducing the desired distribution.

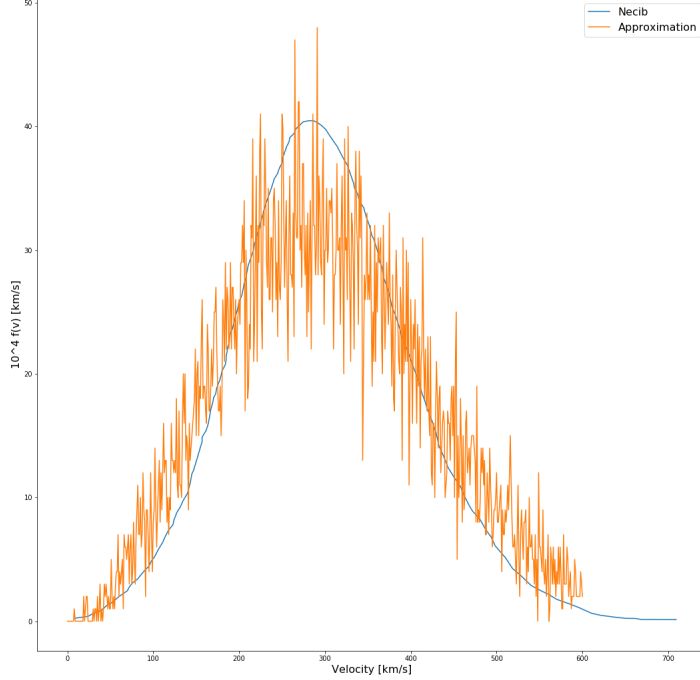


Figure 8. A velocity distribution generated from the approximation for the Necib model used in the simulation is laid over the Necib PDF for comparison.

The simulation now attempts to assign velocities to the particles randomly sampled from this distribution, using the following method, which is a numerical variation of the inverse transform sampling algorithm [75].

First, the cumulative distribution is plotted of the function. This will be normalised so that the maximum value is 1, and takes the form shown.

A pseudo-random number generator then selects a value,  $x$ , uniformly from the interval  $[0,1]$  (how this is done is discussed in the next section). In the true inverse transform sample, the quantile function is generated from this, which constitutes the inverse of the cdf, and then samples found by taking the uniform random variable  $x$  as an input to this function. Though some success has been found recently in approximating the quantile function for the Maxwell-Boltzmann distribution [76], this is at any rate computationally complex. Instead, this value  $x$  is taken as the value of  $F(x)$ , and the simulation runs through the velocities to locate the speed associated with this value of the cdf. This works as a good numerical approximation to the full quantile method.

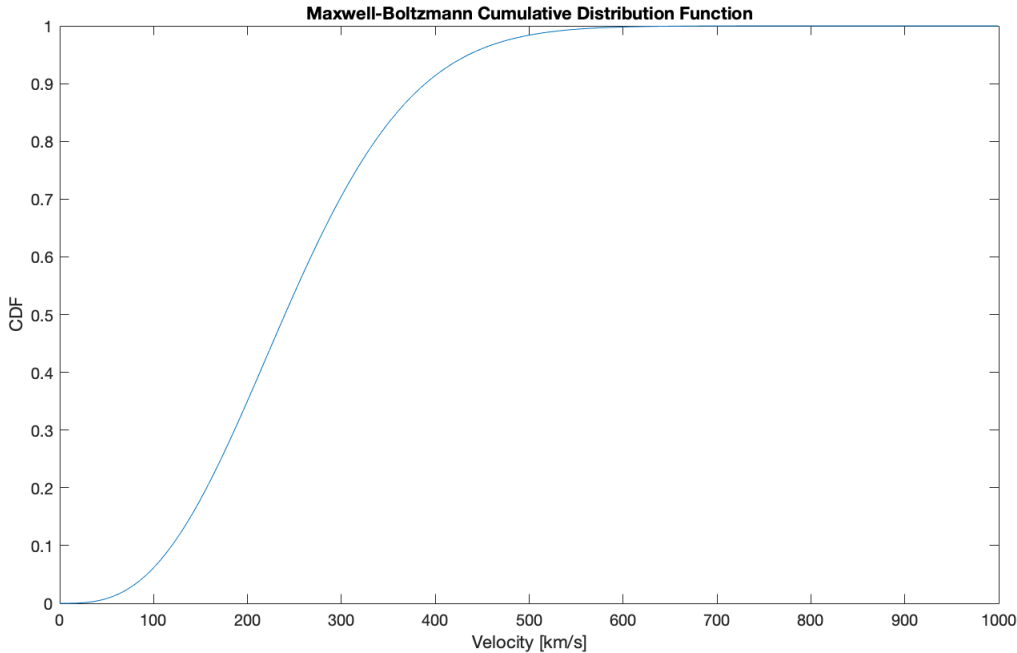


Figure 9. The cumulative density function of the Maxwell-Boltzmann velocity distribution with characteristic speed 220 km/s.

Now, the particles must be assigned a direction in 3D space. This is not trivial, as a straightforward uniformly random generation of angles in spherical polar coordinates in fact ends up biasing the vectors towards the poles, since the area infinitesimal on the surface of some sphere centred on the origin  $d\Sigma = \sin\phi d\phi d\theta$  is a function of  $\phi$ . There are a variety of methods to circumvent this, but the one chosen utilises the unbiased nature of the unit cube.

For each particle, three uncorrelated randomly-sampled numbers in the interval  $[0,1]$  are generated, as before. Then these are assigned as the coordinates of points evenly distributed throughout the cube. By taking the distance of each point from the origin and sampling out any whose length is greater than 1, a unit sphere is left with points evenly distributed throughout. These are now unbiased. By renormalising the distance of each of these points from the origin and taking them as unit vectors, evenly distributed unit vectors are returned.

The simulation then combines the x,y and z components of these unit vectors with the magnitude of the velocity calculated previously for each WIMP, to store an N-body register of WIMP velocities. This sampling is, to this point, isotropic.

### 3.4 Galilean Transformation

Since the velocities in question are non-relativistic, a Galilean transformation can now be performed to interpret the WIMP velocities from the frame of the Earth. For this purpose,

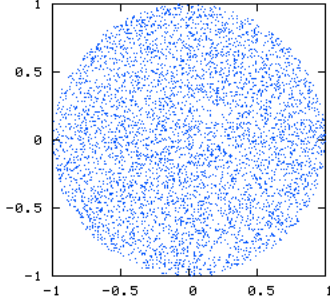


Figure 10. A cross section of points sampled randomly from the unit sphere, courtesy of [77]. In the simulation this is found by sampling the entire unit sphere then removing those lying beyond a distance of 1 from the origin.

the method used takes the propagation of the sun in its orbit of the Milky Way as constant, and factors the phase of the Earth’s orbit of the sun into the transformation as a function of time.

This transformation now invalidates the isotropy of the system, and a coordinate system must be set. For this, the I.A.U galactic coordinate system is used [78]. In practical terms, this means that the sun is taken to propagate in the z-direction, with x pointing towards the galactic centre and y vertically out of the galactic plane. The following equations defining the transform are laid out by Copi & Krauss [79].

$$v_x^E = v_x^G - 0.13v_{sun}\sin(2\pi\Delta t) \quad (9)$$

$$v_y^E = v_y^G + 0.11v_{sun}\cos(2\pi\Delta t) \quad (10)$$

$$v_z^E = v_z^G - v_{sun}(1.05 + 0.06\cos(2\pi\Delta t)) \quad (11)$$

$$(12)$$

$$\Delta t = \frac{t - t_0}{T} \quad (13)$$

Where  $v_{sun}$  is the velocity of the sun in its orbit of the galaxy, taken to be 220 km/s,  $\Delta t$  tracking the fraction of Earth’s orbit covered since the reference day  $t_0$  of 2nd June, the 153rd day of the year.

For the subsequent simulation, the time of year is set to reference 1st January, though this of course can be varied. The effect of this transformation is to smear the velocity distribution as shown below.

### 3.5 Yield

The simulation is now able to generate a store of N particles randomly sampled from the appropriate distributions. To determine the number of particles to simulate, the detector

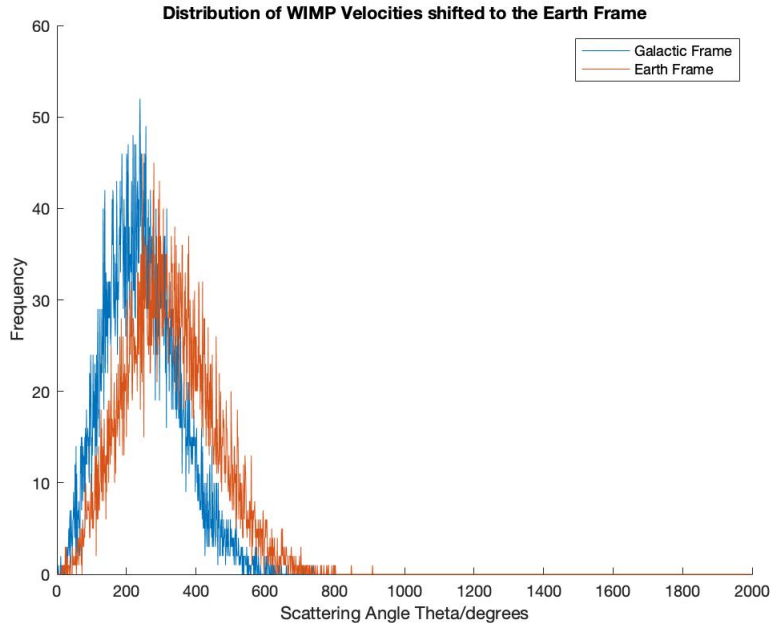


Figure 11. A comparison of the WIMP velocity distribution estimated for both the Galactic and Earth Frames.

dimensions and the anticipated density of dark matter are used to define a flux of WIMP particles through the detector.

The relic density inferred for the WIMP fixes its mass density, and so the WIMP mass has a direct relationship with the number density and therefore the flux through some area. The yield for a generic process is calculated through the following equation:

$$R = n_b \Phi_a \sigma \quad (14)$$

Where R is the yield, often referred to as the interaction rate,  $n_b$  is the number of target nuclei,  $\Phi_a$  is the flux of incident particles and  $\sigma$  is the cross section inherent to the interaction. If the flux is replaced by the flux density of particles per second, this now equates to the interaction rate of the process. Note that the two floating variables here are the WIMP mass and cross section, with the mass having an inverse relationship to the interaction rate and the cross section being directly proportional.

The simulation assumes the specification of the LUX detector, and so the simulation reads in the 90% confidence limit data for spin-independent WIMP-nucleon cross section from this experiment [8], which maps values for the WIMP mass to the corresponding cross section required to generate a number of detectable events in line with measurement. This serves to factor in the constants in the above equation, as well as incorporating the effect of the detector efficiency. Note that at low mass, the cross section rises rapidly to maintain the same interaction rate; this occurs because the detector becomes increasingly ineffective at

detecting collision events at this range of masses, and so the cross section of the interaction must increase to accommodate this.

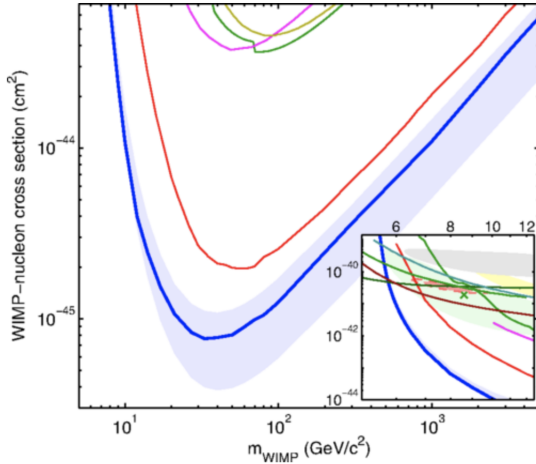


Figure 12. The LUX WIMP-nucleon cross section mapping. The blue line represents the 90% confidence limit on the number of detected signal events.

The simulation now needs to process the above data in order to generate an interaction rate for a given combination of WIMP mass and cross section. A calibration variable is generated as a function of the WIMP mass like so:

$$\lambda = \frac{2.3}{\frac{\sigma}{m_W}} \quad (15)$$

In other words, the proportionality factor linking the raw input variables for the interaction rate are compared to observation, and this value is assigned to the range of masses. Then any unconstrained pair of masses and cross sections can be input to give an expected yield, like so:

$$R = \lambda \frac{\sigma}{m_W} \quad (16)$$

This value then defines the expectation of a randomly sampled number of events  $N$  that is produced by the simulation. Thus, for a given configuration there is a finite probability of no signal events occurring. The method by which this sampling is performed is discussed in the next section.

Again, a similar method to that used for the velocities is used to sample from the yield distributions. This is taken to obey Poisson Statistics, and so for  $R < 20$ , the probability mass function for the corresponding Poisson distribution is calculated .

$$f(n) = \frac{\lambda^n e^{-\lambda}}{n!} \quad (17)$$

The simulation numerically sums these to arrive at a cdf, and again samples from this distribution using the same numerical analog to the inverse transform sampling method discussed in Particle Generation.

For larger values, the Poisson Distribution becomes inefficient to compute; in particular the presence of the factorial function in its probability mass function poses a problem beyond 13 as its value cannot be stored outright on a 32-bit register<sup>9</sup>. The Central Limit Theorem dictates that the distribution will more closely resemble the Normal Distribution as the mean value rises, and so a reasonable cutoff of 20 was chosen beyond which the value is randomly sampled from a Gaussian curve  $N(\lambda, \lambda)$ .

A system clock-generated random number is provided to sample from this distribution, and the resulting value is fed to the simulation to set the lengths of the dynamic arrays for the sample distribution. As the ultimate aim is to compare this sample to some large dataset, a second dataset is generated with an arbitrarily large number of entries of 10,000. These undergo to sampling described above to set their velocities.

### 3.6 Kinematics

The simulation of collision events assumes non-relativistic elastic scattering. Both conditions are well supported by the range of velocities in question and the particles involved respectively [80].

Crucially, the simulation devised makes use of the symmetry of the scattering events considered to neglect variables that will not influence the end result. For instance, no distinction need be made for the direction from which a simulated WIMP hits the detector; since it is the recoil energy of the target that is measured, only the magnitude of its velocity and the angle through which it scatters is relevant.

In the same way, all scattering events will be analysed only in one plane, as due to conservation of momentum it is always possible to express the kinematics in two dimensions and thus disregard the third coordinate set. As such, all collision events can be fully represented by the angles of scatter,  $\theta$ , the angle of recoil,  $\phi$  and the three relevant velocities.

The following angles are defined as below, so that all angles take values over the range [-180,180]. Thus maximum scattering occurs at the edges of the range and 0 degrees represents an uninterrupted propagation of the WIMP.

First consider the centre of momentum frame for a given collision between the Xenon nucleus and an incident WIMP. By choosing this frame, the two particles are fixed to collide head-on, and the scattering angle  $\theta$  can be taken to be uniformly random, as any given configuration returns the same energies and is thus equally probable. The WIMP and the nucleus then separate in opposite directions with equal momentum (due to elasticity).

---

<sup>9</sup>This was solved in the simulation by avoiding calculating the factorial outright, and instead applying its calculation in stages

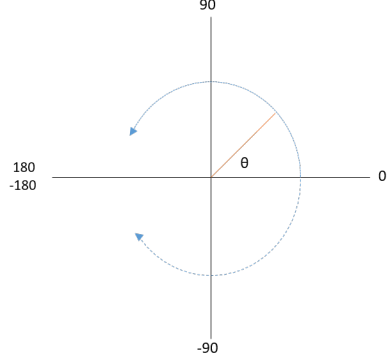


Figure 13. The convention used to define angles in scattering events as the one above.

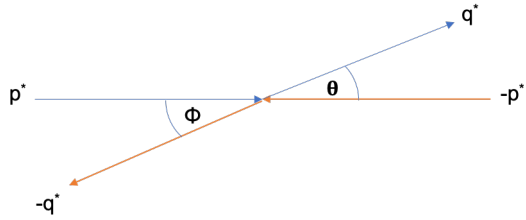


Figure 14. A basic layout of the Centre of Momentum frame scattering. Note that  $|p| = |q|$  due to the choice of frame, and all angles of scattering in this frame are kinematically identical.

In the same way as was encountered when sampling the WIMP unit vectors, it is not trivial to select angles uniformly and a similar method is used here. Now only a 2D plane need be considered, and so numbers are randomly sampled in the interval  $[-1,1]$  twice and combined to a 2D vector, effectively sampling from a unit square. By removing any point that lies further than 1 unit from the origin, this now becomes a sample from the unit sphere. By scaling these points by their length, there are now uniform randomly sampled points on the unit circle, which can provide a uniform distribution of scattering angles. Of course the experiment will be analysed from the laboratory frame where the Xenon nucleus is taken to be at rest, which will resemble the below.

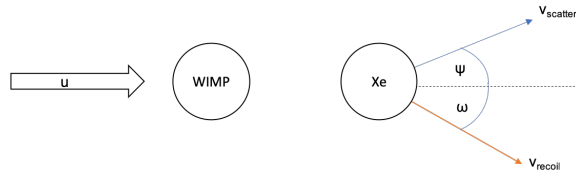


Figure 15. A diagram of the scattering event in the lab frame.

In this frame, the scattering angle  $\theta_L$  can be found by performing a Galilean transformation to the centre of momentum frame, which takes the following form:

$$\tan \theta_L = \frac{\sin(\theta_{cm})}{\cos(\theta) + \frac{M_w}{M_X}} \quad (18)$$

where  $\theta_L$  is the lab frame scattering angle,  $\theta_{cm}$  is the centre of momentum scattering angle,  $M_W$  is the WIMP mass and  $M_X$  is the Xenon nucleus mass. This acts to narrow the range of scattering angles, dependent on the expected WIMP mass. A heavy WIMP leads to a more narrowly distributed set of small angles, whereas a lighter WIMP can maintain a large range. This is shown below for a WIMP mass of  $100 \text{ GeV}/c^2$ , whilst the Xenon nuclei is of course  $132.9 \text{ GeV}/c^2$

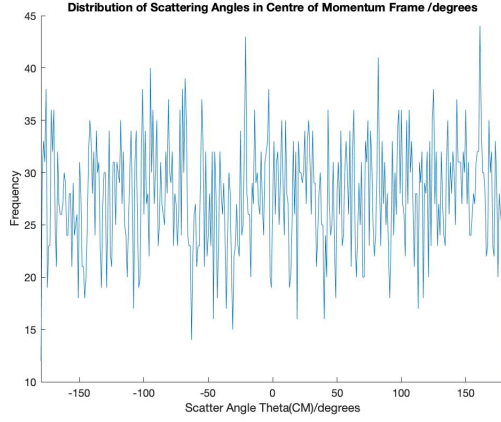


Figure 16. The generated distribution of Centre of Momentum Angles, spread uniformly over the range [-180,180].

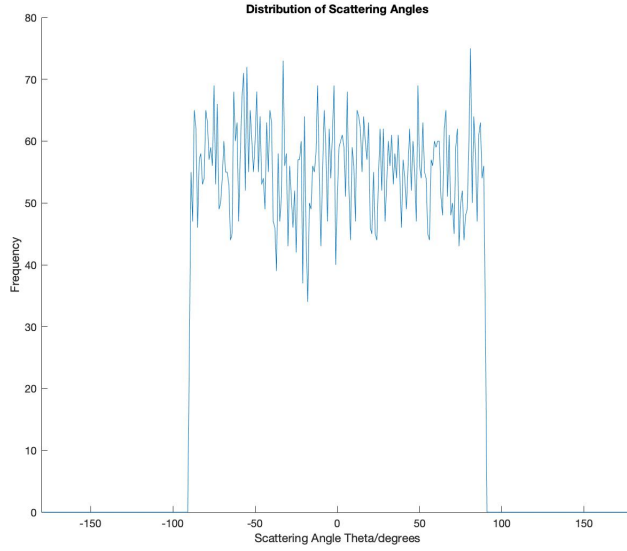


Figure 17. The scattering angles in the laboratory frame confined to the range [-90,90]. This makes sense as it would be unphysical for a WIMP to collide with a stationary nucleus and for the nucleus to recoil in the opposite direction.

Quantifying the angle of scatter and recoil allows the post-collision velocities to be calculated via conservation of momentum and energy. This was performed like so:

$$v_R = u \frac{m_W}{(m_X + m_W)^2} \sqrt{2 - 2\cos(\theta_{CM})} \quad (19)$$

Where  $u$  is the initial velocity and  $v_R$  is the recoil velocity. Likewise, for consistency the scattering velocity could be found via;

$$v_S = u \frac{m_W}{m_X} \left( 1 + \frac{m_W}{m_X} \right) \sqrt{(1 - \cos\theta_{CM})^2 + \sin^2\theta_{CM}} \quad (20)$$

From these, it is then straightforward to calculate the corresponding energies simply by using  $E = \frac{1}{2}mv^2$ .

### 3.7 Detector Flaws

Characteristically for a given detector there is some relation between the detected energy and the true energy deposited, known as the 'quenching factor'. This is given below:

$$\frac{dR}{dE_R} = f_n \left( 1 + \frac{E_R}{f_n} \frac{df_n}{dE_R} \right) \frac{dR}{dE_v} \quad (21)$$

[46]

Where  $R$  is the interaction rate,  $E_R$  is the recoil energy,  $E_v$  is the detected energy deposited and  $f_n$  is the WIMP-neutron coupling [46]. The neutron coupling arises as elastic scattering at low energy from neutrons is anticipated to occupy the same phase space as prospective WIMPs interactions, and so they are easily mistaken for the anticipated signal. A given detector will attempt to infer this relationship from known interactions and correct for it.

Similarly, direct detectors are expected to have an ionisation/scintillation efficiency that falls as the energy deposited reduces [67]. In fact this was already seen simply from observing the LUX yield data (Figure 12); WIMPs at lower masses were much harder to measure, which led to the rising estimated value of the cross section at low mass. Indeed, there will be some threshold of energy required to initiate ionisation [46], which will lead to a sharp drop in detection at smaller values.

The phenomena discussed in this section will all act to modify the observations of the true recoil spectra from direct detectors. However, it seems reasonable that a calibration introduced across the data to account for the efficiency would consistently modify the data between samples, and so can be omitted for the purpose of the statistical analysis and to reduce the level of computation required.

## 3.8 Measurement Corrections

To fully capture the true outputs, a variety of factors that influence real detectors must be accounted for. These are chiefly as follows.

The detector will inevitably be in propagation: on Earth, the movement of the sun and Earth must be considered as this will affect the observed velocity distribution. This was encoded by performing simple Galilean transformations to the characteristic Maxwell-Boltzmann velocities of the simulated WIMPs.

The measured recoil energy at the detector will differ from the true value due to the resolution of the detector. This can be modelled reasonably by considering the measured value for some energy reading to be sampled from a Gaussian distribution centred on the 'true value', with the width of this distribution quantified by some detector resolution parameter  $f$ . The result of this would be a 'smearing' of the resulting data. This effect was not directly incorporated into the simulation, as it is not clear to what degree it would alter any of the analysis applied between distributions and would involve a substantial increase in the computation required.

There will likewise be a form factor dependent on the energy of the collision that moderates the matrix element of the interaction. This was introduced in the theory section. The form factor masks the recoil energy spectrum by suppressing interactions at some energies. Models of WIMP-Xenon interactions suggest that destructive interference takes place at recoil energies of around 100 keV (and periodically at higher energies) and can suppress interactions at specific values by seven orders of magnitude [46], so this is clearly an important element of the experiment to reflect. However, in order to produce results in the time frame given, the simulation for now leaves out the implementation of a form factor scaling, though the momentum data required is currently stored ready for this usage.

## 3.9 Statistical Analysis

The statistical analysis used relies on two main steps. The first utilises the K.S Test, which defines the degree to which the recoil spectrum generated resembles that of the target dataset. There is however another piece of information from the sample that can help to distinguish it; the total number of events detected. Thus the second step is to find the probability of observing  $N$  events, given that the sample does derive from the same distribution as the target.

Once the recoil spectra are provided for a given configuration, the K. S. Test can be implemented via the following approach. Recall that, at this point, there are two datasets: the target - a large number of events sampled from the characteristic Maxwell-Boltzmann distribution with the conventional corrections made, and the sample - a small dataset generated with some mass and cross section selected from the phase space.

First, the recoil energy data was ordered from lowest energy to highest. The sorting algorithm used searches through the array and places each entry above or below the previous after comparing their value.

Now in ascending form, the following equation could be used to compute the empirical distribution function for a given value of x:

$$F_{obs}(x_i) = \frac{i}{N} \quad (22)$$

where  $x_i$  is the datapoint at position i in the ordered list and N is the total length of the list. In other words, this function gives the proportion of data  $< x$ .

Now, the absolute difference between the empirical distribution functions arising for each dataset is computed at all points along the interval [0,1]. The algorithm then takes the maximum distance found, which defines the statistic  $D_n$ , and calculates from it the corresponding p-value. This depends on the lengths of the two datasets, and calculates the first 100 terms of the associated Kolmogorov distribution, which was deemed more functionally versatile than attempting to store table values. Consult Marsaglia in [70] for more detail on the expansion. This takes the basic form shown below:

$$P(D_n < D_{obs}) = \sum_{i=1}^{100} 2 \exp \left( 2i^2 \sqrt{\frac{N_1 N_2}{N_1 + N_2}} D_{obs} \right) \quad (23)$$

for a maximum distance  $D_{obs}$ , and sample lengths  $N_1$  and  $N_2$ .

This returns some probability based on the energy spectrum shape. The second step in the statistical analysis can now be factored in. The probability desired is  $P(N = N_{obs})$ , given that this is sampled from a Poisson distribution where  $\lambda$  is the 'true' value in the large dataset, here  $9 \times 10^{-45}$ . This is calculated by computing  $f(N_{obs})$  for the pdf associated with the target dataset yield distribution, then normalising this against the probability of achieving the mean value for the distribution. This means that, should the sample contain the same number of events as that expected from the target dataset, the sample will be allocated 1.0. If the expected yield from the target is 10, a sample of length 1 will be returned a value of 0.125, for example

Multiplied together, this provides a value for the probability that the sample in question is drawn from the underlying distribution based on both its recoil spectrum shape and the event rate. Both the total number of events observed and the recoil energy spectra generated from them provide information about the WIMP distribution independently, though they are of course linked in a very fundamental way.

Since the distributions are generated pseudo-randomly, and in order to find a reliable K.S statistic at each point in the phase space for comparison, this analysis is performed consecutively on 50 iterations for each configuration, and the mean p-value taken. At each iteration the seed for random number generation resets and so the spectrum generated varies, so statistical variation in the K.S values calculated is expected.

This is ultimately performed as a  $100 \times 100$  grid search of the two-dimensional logarithmic phase space created by the WIMP mass and the WIMP-nucleon cross section. This extends

from  $10 - 4,800 \text{ GeV}/c^2$  in mass and  $2 \times 10^{-45}$  to  $10^{-43} \text{ cm}^2$  in cross section. Note that this also extends slightly beyond the anticipated lower WIMP mass limit set in [49] as a conservative approach to ensuring the full range of possible values is covered.

The second stage of analysis is now performed by conducting the above with the samples now being drawn from the approximated form of the Necib model.

## 4 Results and Discussion

### 4.1 P-Value Analysis

The simulation was able to populate a  $100 \times 100$  logarithmic phase space in WIMP mass and cross section with calculated p-values. Recall that the p-value provides a probability that the two samples in question are drawn from the same distribution. This will serve to both quantify the ability of the experimental data to distinguish the WIMP mass and cross section detected, and to identify the influence of the uncertainty in the velocity distribution on this.

Two target datasets were used in the following analysis, though any point in the phase space is a candidate for this. These are constructed with  $m_W = 100 \text{ GeV}/c^2$ ,  $\sigma = 9 \times 10^{-45} \text{ cm}^2$ ; and  $m_W = 60 \text{ GeV}/c^2$ ,  $\sigma = 4 \times 10^{-44} \text{ cm}^2$ , with a mean yield of 13.8 and 66.7 respectively.

#### 4.1.1 Standard Halo Model Grid Search

From Figure 18, observe that the vast majority of the phase space returned p-values  $\sim 0$ , which is testament at least to some degree of ability of direct detection to bound the possible range of WIMP masses and cross sections. Many of these zero values arose as the algorithm failed to fully converge on a value for the D-statistic, though this at any rate reflects that the two distributions under consideration showed very little agreement. Noticeably, this graph demonstrates that, despite this, the simulated measurements could still correspond to a wide variety of masses and cross sections with significant agreement. This will be explored further below.

The above shows the region in phase space that is seen to match the target. Note that the target lies, as expected, among matching datasets. However, the range of qualifying masses extends from around  $10.6$  to  $110 \text{ GeV}/c^2$ . This would suggest that the mass resolution based on this measurement is low. This appears to be true only in this low cross section region, as the mass ranges at higher values are much more sharply peaked. The likely cause of this may simply be the low statistics that characterise recoil spectra in this range (with mean yields  $\sim 2\text{-}5$ ), as these plots will all consist of only a handful of events. As such it will be very hard to discriminate between these datasets. If valid, this would suggest that direct observation of a handful of WIMP signals would likely only be able to bound the WIMP mass for a cross section in this region within one order of magnitude.

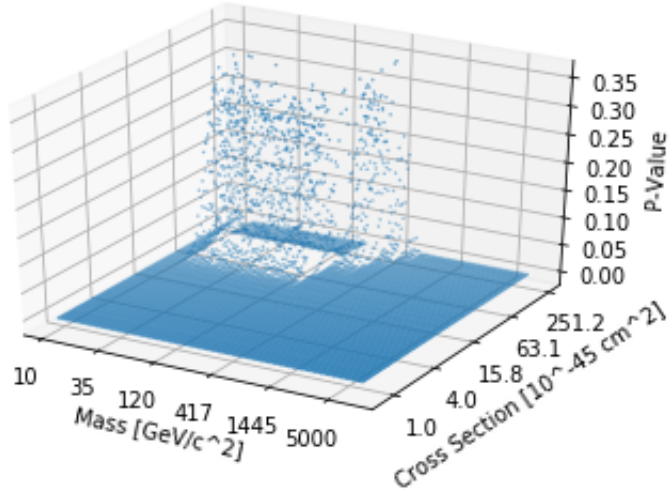


Figure 18. A 3D representation of the mean p-value data with respect to the mass and WIMP-nucleon cross section, for an SHM distribution sample and target  $m_W = 60\text{GeV}/c^2$ ,  $\sigma = 4 \times 10^{-44}\text{cm}^2$

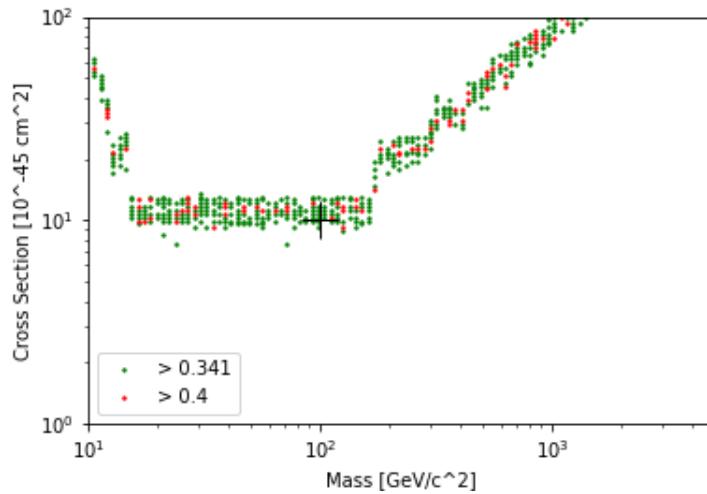


Figure 19. The matched region for the SHM model data, target  $m_W = 100\text{GeV}/c^2$ ,  $\sigma = 9 \times 10^{-45}\text{cm}^2$ . The target is located in the phase space by the black cross.

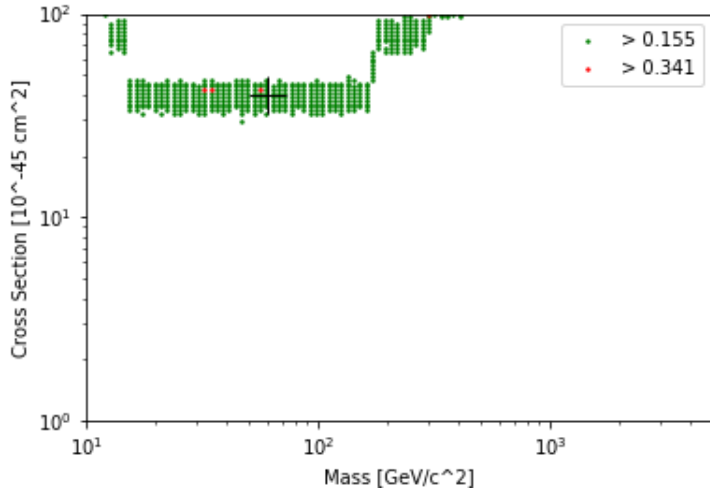


Figure 20. The matched region for the SHM model data, target  $m_W = 60\text{GeV}/c^2$ ,  $\sigma = 4 \times 10^{-44}\text{cm}^2$ . The target is located in the phase space by the black cross.

This observations holds true for the other target dataset, for a near identical range of masses. This suggests that the mass resolution is similarly accurate (or inaccurate) across the phase space, although it would be important to explore a much wider range of target regions to assert this fully. Repeating this analysis for further target datasets would reveal whether this mass resolution holds some fixed relationship to the underlying WIMP mass and cross section. The corresponding observation for the cross section indicates that the datasets appear to be able to specify the cross section within  $\sim 20\%$  of its value. This of course cannot be quantified with any great reliability at this stage, as with the choice of two targets and no obvious relationship between their results, it would be ineffective to do so. The number of events recorded will almost certainly be a factor, as the low sample size inevitably introduces a large degree of statistical variation. To some degree this is the major problem permeating throughout direct detection.

A clear tail forms diagonally upwards to the right of the space for both targets, which mirrors the shape of the mass/cross section yield curve seen in Figure 12. This likely corresponds to the datasets that return similar yields to the target dataset, with high event rate agreement. Similarly, a more narrow bar of matching samples is observed on the left. Again this seems to follow the shape of the yield curve.

An immediate worry at this point was whether the p-value analysis disproportionately selects for the event rate of a sample over its recoil spectrum shape. The code was combed for any error in the processing of the recoil spectra in case this had been the cause, but all of the intermediate outputs were being processed correctly. Nevertheless, it might be that the statistical methodology used in this project happens to be much more sensitive to changes in event number than to the kinematics. Indeed, as mentioned above, it is likely that when considering a target dataset with a low mean yield, the mass resolution suffers simply because there is a small sample size with which to detect the recoil spectrum shape. This could be explored by testing the phase space with targets at a much higher cross section and

comparing the mass resolution. The other choice of target used in this project appeared to react the same regardless of having a much higher mean yield, but the two are very likely not descriptive of the whole phase space.

#### 4.1.2 Necib Model Grid Search

Now consider the plots generated from the Necib model, shown below. For the  $m_W = 60 \text{ GeV}/c^2, \sigma = 4 \times 10^{-44} \text{ cm}^2$  target, there is not quite parity between the two representations; the magnitude of the p-values achieved using the Necib model was lower overall, and so the thresholds are reduced to show the same proportion of data in order to assess the relative shapes. This is expected as the target and sample now differ fundamentally, and so are expected to return lower p-values.

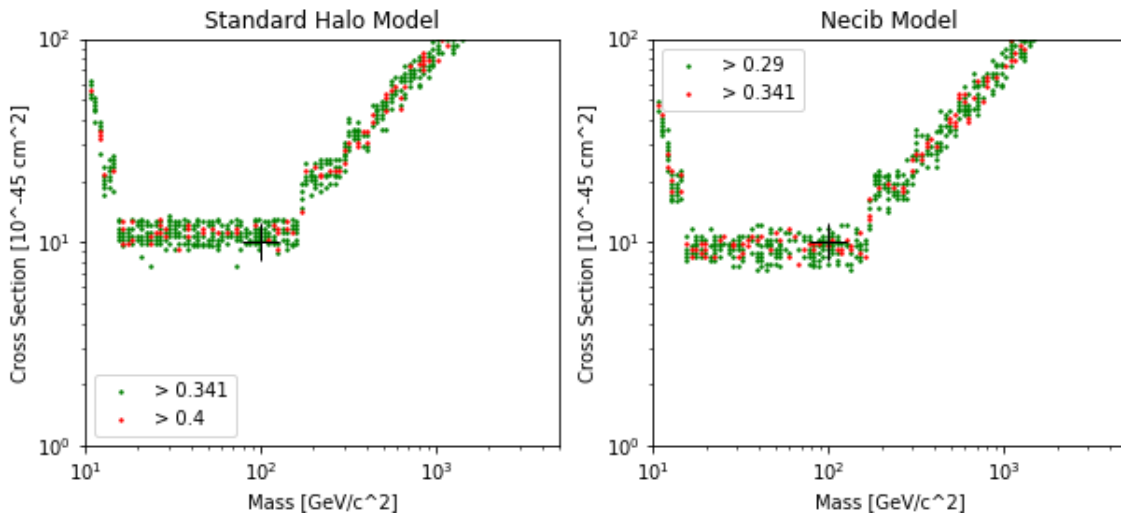


Figure 21. A plot of the matched region in the phase space for both velocity distributions,  $m_W = 100 \text{ GeV}/c^2, \sigma = 9 \times 10^{-45} \text{ cm}^2$ . The target is located at the black crosshairs.

Pleasingly, the same overall shape is shown. Notice that the acceptance region is now shifted downwards to lower cross sections for samples drawn from the Necib model. The values do not appear however to have moved with respect to the mass. At first glance this appears to justify the existence of a systematic error on the WIMP-nucleon cross section in proportion to the vertical movement, but is inconclusive about how this may impact the mass resolution.

When considering the second choice of target, the following pattern is shown. Here the p-values are such that like-for-like can be compared, and in fact the Necib model appeared to show better overall agreement than that for SHM. This is surprising, especially as this choice of target leads to larger sample sizes which should better distinguish the recoil spectra. With an increased mean yield, the difference between the two distributions is much less pronounced. Again, this appears to be the opposite relationship that ought be found; with more samples the two distributions would be expected to appear less alike. This may simply be an indication of the magnitude of the problem at hand in interpreting sampled recoil

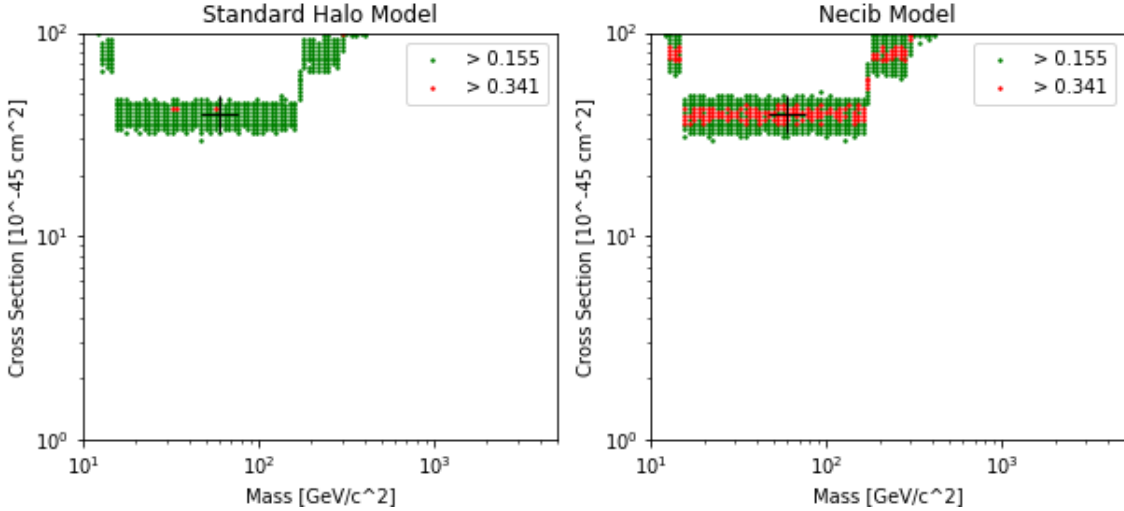


Figure 22. A plot of the matched region in the phase space for both velocity distributions,  $m_W = 60\text{GeV}/c^2$ ,  $\sigma = 4 \times 10^{-44}\text{cm}^2$

data, but perhaps indicates the necessity of increased precision in the simulation to return meaningful results.

#### 4.1.3 Quantifying Systematic Errors

By isolating p-value data along one axis, a direct relationship between the mass/cross section and the agreement with the target can be found. This is shown below.

The two velocity distributions appear to offer no immediate difference in the range of masses identified by the p-value analysis. This does not preclude such a difference, but merely indicates that a more nuanced analysis must be performed to investigate this. It is very likely that modifications to the simulation, such as are discussed in Section 4.2.3, may lead to a possible discrimination between the two curves. Nevertheless, a comparable plot along an axis of constant mass does indicate a shift in the cross section recorded.

Altering the underlying velocity distribution here has shifted the cross sections identified by the K.S test. A simple linear regression algorithm was applied to the two attempting to fit Gaussian curves to the data, and the mean value of these taken as the cross section selected for the samples. The standard deviation of the Gaussian curves then quantify the uncertainty in these values. These gave a cross section of  $1.2(4) \times 10^{-44}\text{cm}^2$  for the SHM data, and  $9(3) \times 10^{-45}\text{cm}^2$  for the Necib model. Based on this, the systematic error in the WIMP-nucleon cross section introduced by the velocity distribution could be estimated at  $3 \times 10^{-45}\text{cm}^2$ , or 25%. Nevertheless, considering the magnitude of the errors in these fits, it is clear that much more analysis would need to be performed to support such an assertion. The most immediate cause of the low confidence in this measurement is likely the low statistics for the recoil spectra in this range. This will inevitably lead to a high level of statistical variance, as one or two outlying events can vastly sway the distribution generated.

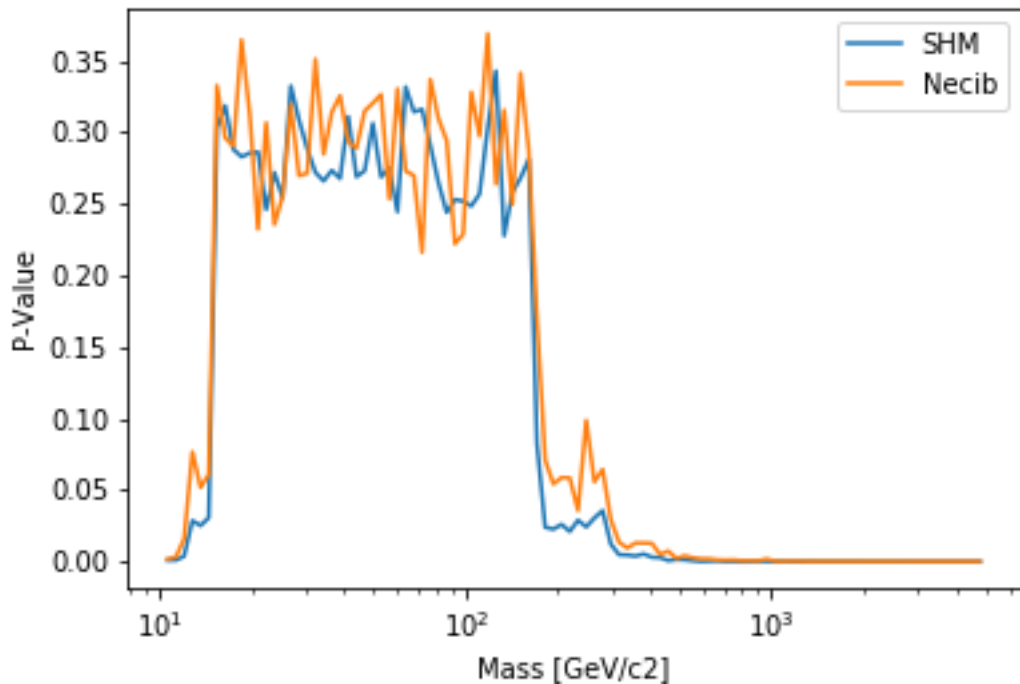


Figure 23. A slice of the p-value data taken at constant  $\sigma = 9 \times 10^{-45} \text{ cm}^2$

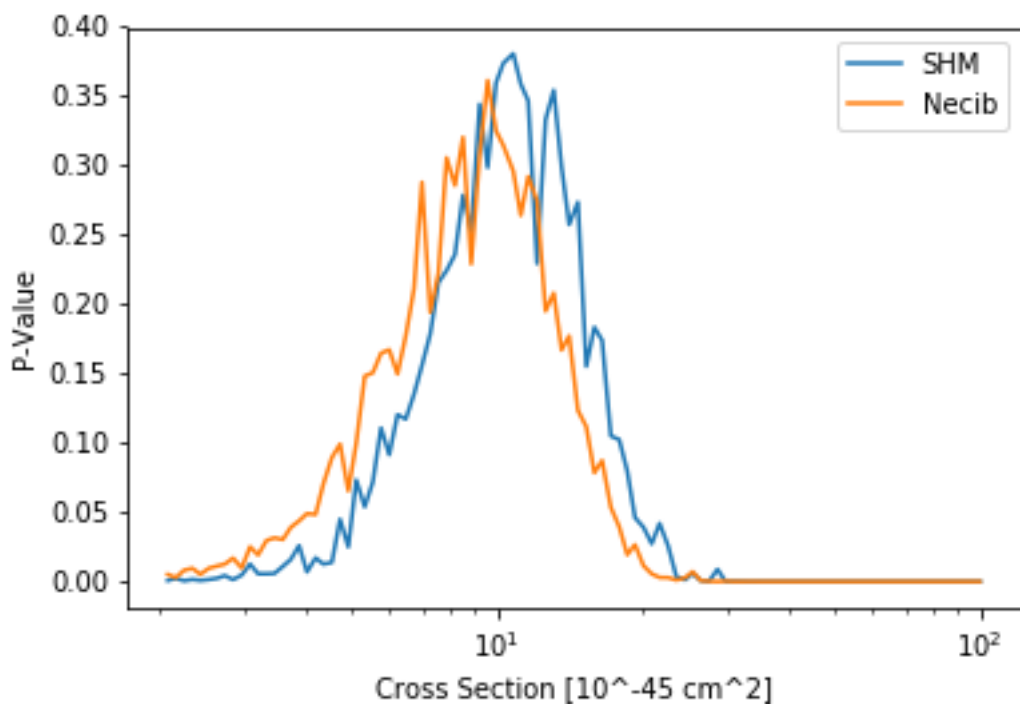


Figure 24. A slice of the p-value data taken at  $m_W = 100 \text{ GeV}/c^2$

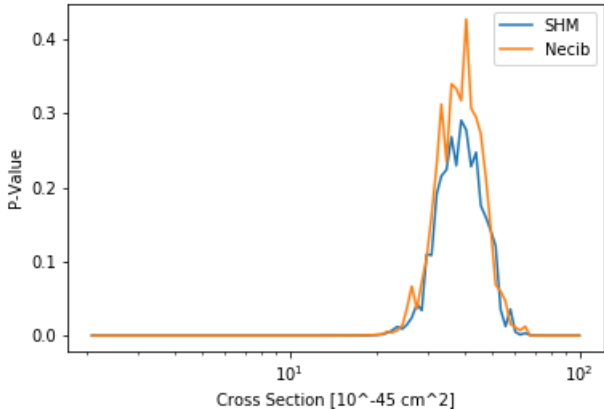


Figure 25. Caption

This distance was also not replicated for the second target, shown in Figure ??.

This demonstrates that if any systematic error were to be found linked to the WIMP velocity distribution, it will very likely hold some relationship with the WIMP mass and WIMP-nucleon cross section assumed in the analysis. Once more this motivates the need for a more thorough scan of the phase space in order to ascertain whether this systematic error is an outlier, or whether it offers a clue as to a more widespread relationship.

#### 4.1.4 Analysis of Statistical Methods

Most of the conclusions drawn above depend heavily on the validity of the statistical analysis applied to the data. It is worthwhile assessing whether there are any drawbacks in the methodology used and where improvements could be made.

Firstly, consider the choice of the K.S test for discriminating mass and cross section. As mentioned previously, it does indeed maintain good validity even at low sample sizes, and in this regard performs favourably to the Pearson  $\chi^2$  test, another non-parametric measure of goodness-of-fit. The two differ fundamentally as the K.S Test is an example of a distance test; it examines the cumulative distribution functions (CDFs) of different distributions [81]. Meanwhile, the  $\chi^2$  Test is an area test, and examines the probability density function (PDF). This measure is less reliable for smaller samples, having low power and a high Type 1 error rate [82], as in this range a reliable distribution cannot be assigned to the test statistic under the null hypothesis. As such,  $\chi^2$  would not appear to be a preferable alternative statistic to use, though there are others.

Similarly, the K.S test is best applied to continuous distributions, and so its application to discrete data may have interfered with its validity [83]. Indeed the K.S test is anticipated to be a conservative estimate of the true p-values [84], and so it is to be expected that the Type 1 error may in fact be recorded here at a lower rate than desired.

A reasonable proposal might be to reattempt the statistical analysis of this data with the Cramér-von-Mises test, which has been shown to be more powerful than the K.S test for some deviations from the null hypothesis [83]. In particular this method would be more sensitive to subtle changes along the entire distribution rather than significant variance over a small range, which may prove more beneficial in this study.

#### 4.1.5 Future Improvements

Ultimately, this project struggles to propose reliable systematic errors arising from uncertainty in the WIMP velocity distribution. There is much scope for future research to build on this.

Of immediate interest would be an attempt to directly use the halo-disk-substructure model calculated by Necib to define the velocity distribution in the simulation, rather than the use of an approximated function as done here. The true Necib velocity profile was generated through simulation (and interpreting the Gaia data) [11], and so the most reasoned approach may be to store the full probability density function in the simulation, rather than attempting to derive some function for it, and randomly sample from this. There will be limitations to how well the current approximation reproduces the desired spectra, and this modification would remove this problem.

Similarly, to more accurately model the contribution of the velocity uncertainty to the spectra identification, it would be useful to compare the SHM spectra to that of a range of velocity distributions continuously varied through the Necib model and beyond. This would involve parametrising the set of velocity distributions that can provide flat rotation curves, and slowly varying a given parameter, recording its p-value scores as this occurs. The peak p-value identified will likely drift away from the target as the distribution moves away from the SHM model, and a relationship between the velocity profile and the accuracy of mass/cross section identification could be found. An estimate generated on these lines would be valid regardless of the specific validity of the Necib model, but would instead characterise a broad range of potential distributions.

An alternative attempt to improve on the validity of the systematic error would simply be to perform this same analysis on a series of pseudo-experimental datasets like the two analysed above, and plot a histogram of the distance in mass or cross section between the SHM and Necib models. A Gaussian peak would be expected to form in this distance, and the mean value of a fit to this Gaussian would provide a more reliable estimate of the uncertainty. This would require significant computation but would provide a much more useful result.

In the same way, this could be extended by recording this data for targets placed throughout the phase space. This would shed light on the relationship that the target chosen may have on the systematic errors; the results so far appear to show that the two are linked, but cannot indicate how.

## 4.2 Simulation Outputs

It is worthwhile to consider the outputs from the program at every stage in order to provide context to the main results above. The various stages of the simulation are assessed below.

### 4.2.1 Yield Simulation

A reasonable place to start is by observing the performance of the yield sampling. The figure below shows the distribution achieved.

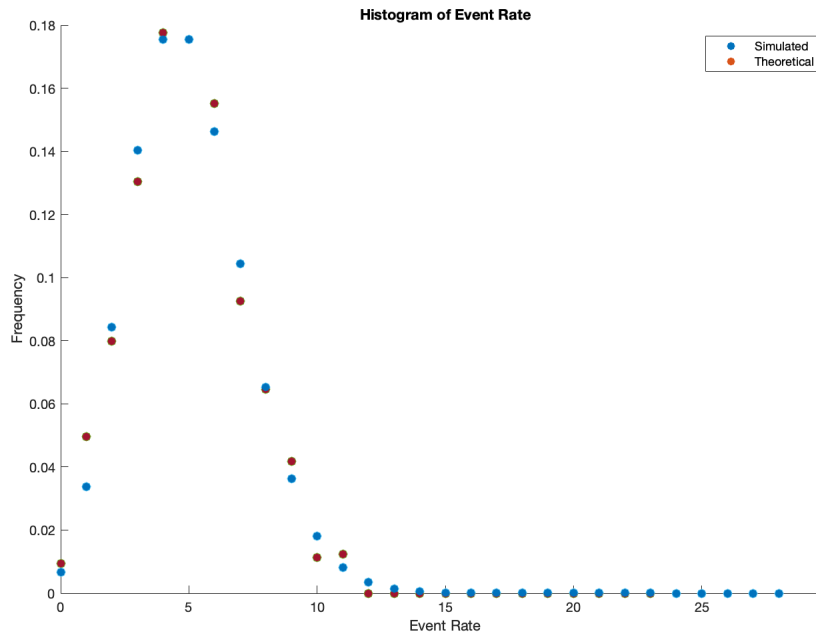


Figure 26. The simulated event rate compared to the theoretical values for a Poisson Distribution with  $\lambda = 5$

The simulation appears to have successfully sampled values at something approximating the desired Poisson distribution. It is hard to distinguish any meaningful pattern in the results that would indicate a systematic error in the simulated data, though the distance from the theoretical results for many points is higher than would be expected of the statistics. This analysis was performed by analysing a 7192-entry dataset. The residuals for this data is shown below, with the error bars calculated assuming Poisson statistics - in other words, the error on the frequency is taken as the square root of the number of counts involved and scaled appropriately.

As is clear above, the residuals appear to be randomly distributed about the theoretical values (their sum is equal to zero at an accuracy on the order of at least  $10^{-13}$ ), and so the simulation at least centres on the correct values. However, the spread of data indicates that

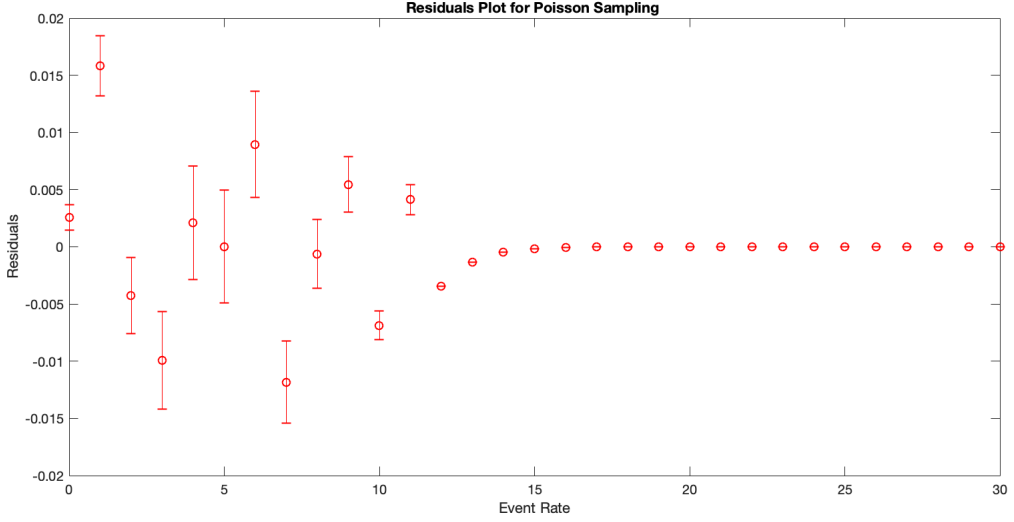


Figure 27. Residuals for the randomly-sampled Poisson distribution data

simple counting statistics vastly underestimates the error in these measurements. It is clear that the algorithm used has a much higher rate of variance than would be expected, which is likely attributable to some systematic error in the simulation.

There are a number of obvious sources for this error. The first potential culprit would be the random number generator, as this has the most immediate power to shift batches of results. The seed for this is set by a modulus calculation on the system clock, which could skew results if multiple entries are deemed to occur within the same second and so are assigned the same random number. This would explain some values being much higher than expected whilst others being much lower. An attempt was made to mitigate this problem by including a 'sleep' command in the generator loop for 1 second between runs so as to separate out the calculations, but this may not deal with the problem fully. The modulus operation used functions as follows:

```

size = 12
factor = 1000 × size = 12,000
n = mod(t, factor)
r = randomseed(n)

```

'size' is set by the system as the number of integers to hold the seed. 't' is the system clock time in seconds. Evidently there is a chance that the same seeds be generated repeatedly if the choice of 'factor' is inappropriate. Having analysed the random number generation directly, the following is obtained:

### 4.2.2 Kinematics

It is worth confirming that the kinematics simulated for the WIMP population is physical and aligns with expectations. The most straightforward means to ensure this was to store the difference in energy recorded before and after the collision events. As the interactions are elastic, these values should lie close to zero. For a sample of 5,000 WIMPs generated by the simulation, the root mean square difference in energy relative to the total energy was 0.007(7) keV. This indicates that the simulation of the collisions was effective in enforcing energy conservation.

On a more qualitative level, a characteristic recoil spectrum was analysed to ensure that it resembled the expected shape. This is shown in Figure 28. This covers the range of energies expected; the kinetic energy of the incident WIMPs is of a similar order, and the recoil energies are distributed lower than this, which is consistent with the energy-post collision being shared between the two particles. The only particular feature of note is that the recoil spectrum gradient is larger than expected to close to zero. This may have been a quirk of the code whereby values were progressively rounded down to zero. The other main culprit would be the propagation of an error with the random sampling of scattering angles or velocities. It is difficult to identify a cause for this as the problem appears not to have significantly altered the rest of the distribution.

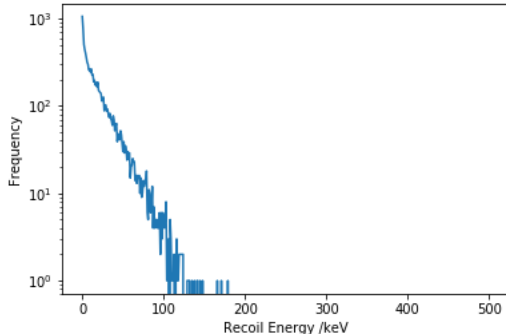


Figure 28. An example recoil spectrum generated for 10,000 events, for the  $100GeV/c^2$ ,  $\sigma = 9 \times 10^{-45}cm^2$

The random sampling that underpins both the scattering angle, velocity and unit vector allocation was limited by the resolution of the spectra used. The program constructed the cumulative distribution function as a discrete array, which will inevitably be imperfect in lieu of the use of a smooth continuous function. This method of course worked well for the Poisson distribution, where only integers need be considered, but for the velocities and angles split the data cdf into bins and used the sum of these bins as an approximation of the area under the pdf. For instance, the velocity sampling used an effective binwidth of 1 km/s. This is reasonably accurate and provides enough resolution for much of the results shown, but may be the root cause of the slight defect in recoil energy.

### 4.2.3 Limitations

The most pressing limitation of this simulation is that it does not incorporate the effects of the form factor into the energy spectra. This will undoubtedly play a pivotal role in the recoil energy distribution, though it is unclear how directly this would have influenced the subsequent K.S p-value analysis. Without evidence of its influence being negligible, however, this poses the most significant flaw in the current simulation. By modulating the yield depending on the recoil energy, the inclusion of the form factor may have aided the statistical analysis in distinguishing between masses more effectively.

A successor would do well to examine how such an extension of the program would influence its conclusions. The raw inputs required for this are present in the code, and would simply need to be applied to the generated energy spectra to moderate the histogram values.

The simulation stopped at adjusting the generated data for a finite detector resolution. This would involve an additional random sampling of data from a Gaussian distribution centred on the 'true' value for each reading, with some width related to the detector resolution. Once again, this has the potential to influence the results gathered here, but with suitably high statistics, and estimating the power of the detectors used, this is unlikely to play a major role in differentiating between velocity distributions.

The use of the measured event rate from the first results at LUX [8] encoded the relationship between WIMP mass, cross section and expected yield. The range of masses considered lay within that covered by LUX, and so no extrapolation was required. Nonetheless, this was done simply by allocating some calibration factor to a given WIMP mass to estimate its yield, then applying the fact that the yield is expected to be proportional to the cross section. In other words, if it was found that a more nuanced relationship existed between the cross section and the yield for any reason, this would not be captured by the simulation. This is likely to not have played a significant role in the simulation but nevertheless would be a reasonable investigation. In order to interpret both the WIMP mass and the cross section to read in the mean event rate, the number of stored datapoints for this would need to be squared and referenced upon each iteration, which has the potential to significantly increase computation.

The program similarly does not attempt to model the imperfect identification of signal events above the background. As explored in Section 2.5, experiments such as LUX possess a variety of means with which to correctly identify signal events, which drastically reduces the background noise. Monte Carlo simulations indicate that these steps ought to be more than adequate to successfully identify the WIMP signal [67]. In fact, only 1 in 180 events detected is expected to be background in this configuration [85]. As such, it made sense to neglect this analysis for the purpose of this simulation.

## 5 Conclusion

As such, this project has seen varied success in achieving its aims. The p-value plot for the SHM model gave a reasonable understanding of the resolution possible for WIMP mass and

WIMP-nucleon cross section based on a single period of measurement from the LUX detector. It appeared that such data is more effective at discriminating observed recoil spectra for the cross section than the mass, which could only be specified within one order of magnitude. Nevertheless, no immediate conclusions can be drawn from this without analysis conducted throughout the phase space, and it may also be necessary to improve upon the simulation in the ways described in the last section for this purpose.

Comparing the Necib model to this appeared to show no significant change in the mass resolution, but did demonstrate a shift in the cross sections identified. This provides evidence for the existence of some systematic error introduced by the uncertainty in the velocity distribution, and motivates further analysis to attempt to quantify this.

Alongside this, the simulation generated has performed robustly and is fit for purpose for future studies. It will be available for use by further groups and contains the necessary features to allow future incorporation of the form factor, which is the next logical extension of this research. A brief set of instructions on how to do this are provided in the appendices.

## References

- [1] Gianfranco Bertone, Dan Hooper, and Joseph Silk. Particle dark matter: evidence, candidates and constraints. *Physics Reports*, 405(5):279 – 390, 2005.
- [2] Gerard Jungman, Marc Kamionkowski, and Kim Griest. Supersymmetric dark matter. *Physics Reports*, 267(5):195 – 373, 1996.
- [3] T Goldman, Juan Pérez-Mercader, Fred Cooper, and Michael Martin Nieto. The dark matter problem and quantum gravity. *Physics Letters B*, 281(3-4):219–224, 1992.
- [4] Douglas Clowe, Marusa Bradac, Anthony H. Gonzalez, Maxim Markevitch, Scott W. Randall, Christine Jones, and Dennis Zaritsky. A direct empirical proof of the existence of dark matter. *Astrophys. J.*, 648:L109–L113, 2006.
- [5] Gianfranco Bertone. The moment of truth for WIMP Dark Matter. *Nature*, 468:389–393, 2010.
- [6] Jonathan H. Davis, Christopher McCabe, and Celine Boehm. Quantifying the evidence for Dark Matter in CoGeNT data. *JCAP*, 1408:014, 2014.
- [7] Tushna Commissariat. Dark-matter searches get us government approval. <https://physicsworld.com/a/dark-matter-searches-get-us-government-approval/>, 2014.
- [8] D. S. et al. Akerib. First results from the lux dark matter experiment at the sanford underground research facility. *Phys. Rev. Lett.*, 112:091303, Mar 2014.
- [9] B. J. Mount et al. LUX-ZEPLIN (LZ) Technical Design Report. 2017.
- [10] Christopher McCabe. Astrophysical uncertainties of dark matter direct detection experiments. *Phys. Rev. D*, 82:023530, Jul 2010.
- [11] Vasily Belokurov Lina Necib, Mariangela Lisanti. Dark matter in disequilibrium: The local velocity distribution from sdss-gaia. *arXiv:1807.02519*, 2018.
- [12] Robert Feldmann and Douglas Spolyar. Detecting dark matter substructures around the milky way with gaia. *Monthly Notices of the Royal Astronomical Society*, 446(1):1000–1012, 2014.
- [13] Katherine Freese. Status of dark matter in the universe. *International Journal of Modern Physics D*, 26(06):1730012, 2017.
- [14] F. Zwicky. Die Rotverschiebung von extragalaktischen Nebeln. *Helvetica Physica Acta*, 6:110–127, 1933.
- [15] Virginia Trimble. Existence and nature of dark matter in the universe. *Annual review of astronomy and astrophysics*, 25(1):425–472, 1987.
- [16] ESA NASA and P. van Dokkum (Yale University. Dark matter goes missing in oddball galaxy. [http://hubblesite.org/news\\_release/news/2018-16](http://hubblesite.org/news_release/news/2018-16), March 2018.

- [17] Gibor Basri. Observations of brown dwarfs. *Annual Review of Astronomy and Astrophysics*, 38(1):485–519, 2000.
- [18] Chris G Tinney. The dark matter implications of brown dwarfs. In *The Third Stromlo Symposium: The Galactic Halo*, volume 165, page 419, 1999.
- [19] J. H. Oort. The force exerted by the stellar system in the direction perpendicular to the galactic plane and some related problems. *Bulletin of the Astronomical Institutes of the Netherlands*, 6:249, August 1932.
- [20] SM Kent and JE Gunn. The dynamics of rich clusters of galaxies. i-the coma cluster. *The Astronomical Journal*, 87:945–971, 1982.
- [21] Jeremiah P Ostriker, PJE Peebles, and Amos Yahil. The size and mass of galaxies, and the mass of the universe. *The Astrophysical Journal*, 193:L1–L4, 1974.
- [22] M. Azzaro, F. Prada, and C. M. Gutierrez. Motion properties of satellites around external spiral galaxies. *ASP Conf. Ser.*, 327:268, 2004.
- [23] Mario Mateo. Dwarf galaxies of the Local Group. *Ann. Rev. Astron. Astrophys.*, 36:435–506, 1998.
- [24] W. J. G. de Blok, Stacy S. McGaugh, Albert Bosma, and Vera C. Rubin. Mass density profiles of LSB galaxies. *Astrophys. J.*, 552:L23–L26, 2001.
- [25] Richard Hammond. *The Unknown Universe: The Origin of the Universe, Quantum Gravity, Wormholes, and Other Things Science Still Can't Explain*. New Page Books, 2008.
- [26] Edvige Corbelli and Paolo Salucci. The Extended Rotation Curve and the Dark Matter Halo of M33. *Mon. Not. Roy. Astron. Soc.*, 311:441–447, 2000.
- [27] Edvige Corbelli and Paolo Salucci. The extended rotation curve and the dark matter halo of M33. *Monthly Notices of the Royal Astronomical Society*, 311:441–447, January 2000.
- [28] P. Salucci and A. Borriello. The intriguing distribution of dark matter in galaxies. *Lect. Notes Phys.*, 616:66–77, 2003.
- [29] D. N. Spergel, R. Bean, O. Dore, M. R. Nolta, C. L. Bennett, J. Dunkley, G. Hinshaw, N. Jarosik, E. Komatsu, L. Page, H. V. Peiris, L. Verde, M. Halpern, R. S. Hill, A. Kogut, M. Limon, S. S. Meyer, N. Odegard, G. S. Tucker, J. L. Weiland, E. Wollack, and E. L. Wright. Three-Year Wilkinson microwave anisotropy probe(WMAP) observations: Implications for cosmology. *The Astrophysical Journal Supplement Series*, 170(2):377–408, jun 2007.
- [30] Wayne Hu and Scott Dodelson. Cosmic microwave background anisotropies. *Annual Review of Astronomy and Astrophysics*, 40(1):171–216, 2002.
- [31] Simon D. M. White, C. S. Frenk, and M. Davis. Clustering in a Neutrino Dominated Universe. *Astrophys. J.*, 274:L1–L5, 1983. [,80(1984)].

- [32] D. N. Spergel et al. Wilkinson Microwave Anisotropy Probe (WMAP) three year results: implications for cosmology. *Astrophys. J. Suppl.*, 170:377, 2007.
- [33] C. Alcock et al. The MACHO project: Microlensing results from 5.7 years of LMC observations. *Astrophys. J.*, 542:281–307, 2000.
- [34] Edward W. Kolb and Michael S. Turner. The Early Universe. *Front. Phys.*, 69:1–547, 1990.
- [35] Kim Griest and Marc Kamionkowski. Unitarity limits on the mass and radius of dark-matter particles. *Physical Review Letters*, 64(6):615, 1990.
- [36] Leszek Roszkowski, Enrico Maria Sessolo, and Sebastian Trojanowski. WIMP dark matter candidates and searches—current status and future prospects. *Reports on Progress in Physics*, 81(6):066201, may 2018.
- [37] JR Bond and G Efstathiou. Cosmic background radiation anisotropies in universes dominated by nonbaryonic dark matter, 1984.
- [38] G. Blanger, F. Boudjema, A. Pukhov, and A. Semenov. micromegas2.0: A program to calculate the relic density of dark matter in a generic model. *Computer Physics Communications*, 176(5):367 – 382, 2007.
- [39] Gian F Giudice, Edward W Kolb, Antonio Riotto, Dmitry V Semikoz, and Igor I Tkachev. Standard model neutrinos as warm dark matter. *Physical Review D*, 64(4):043512, 2001.
- [40] Robert Resnick David Halliday and Jearl Walker. *Principles of Physics*. John Wiley Sons, 2014.
- [41] Gerard Jungman, Marc Kamionkowski, and Kim Griest. Supersymmetric dark matter. *Phys. Rept.*, 267:195–373, 1996.
- [42] DS Akerib, S Alsum, HM Araújo, X Bai, AJ Bailey, J Balajthy, P Beltrame, EP Bernard, A Bernstein, TP Biesiadzinski, et al. Results from a search for dark matter in the complete lux exposure. *Physical review letters*, 118(2):021303, 2017.
- [43] Daniel R Tovey, RJ Gaitskell, P Gondolo, Y Ramachers, and L Roszkowski. A new model-independent method for extracting spin-dependent cross section limits from dark matter searches. *Physics Letters B*, 488(1):17–26, 2000.
- [44] Christopher Savage, Andre Scaffidi, Martin White, and Anthony G Williams. Lux likelihood and limits on spin-independent and spin-dependent wimp couplings with luxcalc. *Physical Review D*, 92(10):103519, 2015.
- [45] DC Mallings, DS Akerib, HM Araujo, X Bai, S Bedikian, E Bernard, A Bernstein, A Bradley, SB Cahn, MC Carmona-Benitez, et al. After lux: the lz program. *arXiv preprint arXiv:1110.0103*, 2011.
- [46] Anthony Hollingsworth. Results from the ZEPLIN-II experiment. Master’s thesis, University of Edinburgh, August 2012.

- [47] S. Pittel J. Engel and P. Vogel. Nuclear physics of dark matter detection. *International Journal of Modern Physics E*, 1, 1992.
- [48] Gary Steigman. CMB Constraints On The Thermal WIMP Mass And Annihilation Cross Section. *Phys. Rev.*, D91(8):083538, 2015.
- [49] Rebecca K. Leane, Tracy R. Slatyer, John F. Beacom, and Kenny C. Y. Ng. Gev-scale thermal wimps: Not even slightly ruled out. *Phys. Rev. D*, 98:023016, Jul 2018.
- [50] Patrick Crotty. High-energy neutrino fluxes from supermassive dark matter. *Physical Review D*, 66(6):063504, 2002.
- [51] J.D. Lewin and P.F. Smith. Review of mathematics, numerical factors, and corrections for dark matter experiments based on elastic nuclear recoil. *Astroparticle Physics*, 6(1):87 – 112, 1996.
- [52] L. Vietze, P. Klos, J. Menndez, W. C. Haxton, and A. Schwenk. Nuclear structure aspects of spin-independent WIMP scattering off xenon. *Phys. Rev.*, D91(4):043520, 2015.
- [53] Julio F Navarro, Carlos S Frenk, and Simon DM White. A universal density profile from hierarchical clustering. *The Astrophysical Journal*, 490(2):493, 1997.
- [54] Yao-Yuan Mao, Louis E. Strigari, and Risa H. Wechsler. Connecting Direct Dark Matter Detection Experiments to Cosmologically Motivated Halo Models. *Phys. Rev.*, D89(6):063513, 2014.
- [55] Simon D. M. White, Volker Springel, Mark Vogelsberger, and Roya Mohayaee. Caustics in growing cold dark matter haloes. *Monthly Notices of the Royal Astronomical Society*, 400(4):2174–2184, 12 2009.
- [56] John March-Russell and Stephen M. West. Wimponium and boost factors for indirect dark matter detection. *Physics Letters B*, 676(4):133 – 139, 2009.
- [57] Ben Moore, Sebastiano Ghigna, Fabio Governato, George Lake, Thomas Quinn, Joachim Stadel, and Paolo Tozzi. Dark matter substructure within galactic halos. *The Astrophysical Journal Letters*, 524(1):L19, 1999.
- [58] Lina Necib, Mariangela Lisanti, Shea Garrison-Kimmel, Andrew Wetzel, Robyn Sanderson, Philip F. Hopkins, Claude-Andr Faucher-Giguere, and Duan Kere. Under the Firelight: Stellar Tracers of the Local Dark Matter Velocity Distribution in the Milky Way. 2018.
- [59] Paolo Gondolo and Joseph Silk. Dark matter annihilation at the galactic center. *Physical Review Letters*, 83(9):1719, 1999.
- [60] CERN. Dark matter. <https://home.cern/science/physics/dark-matter>.
- [61] Mark W. Goodman and Edward Witten. Detectability of certain dark-matter candidates. *Phys. Rev. D*, 31:3059–3063, Jun 1985.

- [62] Mark W. Goodman and Edward Witten. Detectability of Certain Dark Matter Candidates. *Phys. Rev.*, D31:3059, 1985. [,325(1984)].
- [63] Z Ahmed, DS Akerib, S Arrenberg, MJ Attisha, CN Bailey, L Baudis, DA Bauer, J Beaty, PL Brink, T Bruch, et al. Search for weakly interacting massive particles with the first five-tower data from the cryogenic dark matter search at the soudan underground laboratory. *Physical Review Letters*, 102(1):011301, 2009.
- [64] Rodionov B.U. Dolgoshein B.A., Lebedenko V.N. New method of registration of ionizing-particle tracks in condensed matter. *JETP Letters*, 11, 1970.
- [65] Marc Schumann. Dark Matter Search with liquid Noble Gases. 2012.
- [66] Prototype of lux-zeplin dark matter detector tested at slac, 2016.
- [67] D.S. Akerib, X. Bai, S. Bedikian, E. Bernard, A. Bernstein, A. Bolozdynya, A. Bradley, D. Byram, S.B. Cahn, C. Camp, M.C. Carmona-Benitez, D. Carr, J.J. Chapman, A. Chiller, C. Chiller, K. Clark, T. Classen, T. Coffey, A. Curioni, E. Dahl, S. Dazeley, L. de Viveiros, A. Dobi, E. Dragowsky, E. Druszkiewicz, B. Edwards, C.H. Faham, S. Fiorucci, R.J. Gaitskell, K.R. Gibson, M. Gilchriese, C. Hall, M. Hanhardt, B. Holbrook, M. Ihm, R.G. Jacobsen, L. Kastens, K. Kazkaz, R. Knoche, S. Kyre, J. Kwong, R. Lander, N.A. Larsen, C. Lee, D.S. Leonard, K.T. Lesko, A. Lindote, M.I. Lopes, A. Lyashenko, D.C. Malling, R. Mannino, Z. Marquez, D.N. McKinsey, D.-M. Mei, J. Mock, M. Moongweluwan, M. Morii, H. Nelson, F. Neves, J.A. Nikkel, M. Pangilinan, P.D. Parker, E.K. Pease, K. Pech, P. Phelps, A. Rodionov, P. Roberts, A. Shei, T. Shutt, C. Silva, W. Skulski, V.N. Solovov, C.J. Sofka, P. Sorensen, J. Spaans, T. Stiegler, D. Stolp, R. Svoboda, M. Sweany, M. Szydagis, D. Taylor, J. Thomson, M. Tripathi, S. Uvarov, J.R. Verbus, N. Walsh, R. Webb, D. White, J.T. White, T.J. Whitis, M. Wlasenko, F.L.H. Wolfs, M. Woods, and C. Zhang. The large underground xenon (lux) experiment. *Nuclear Instruments and Methods in Physics Research Section A: Accelerators, Spectrometers, Detectors and Associated Equipment*, 704:111 – 126, 2013.
- [68] M. A. Stephens. Edf statistics for goodness of fit and some comparisons. *Journal of the American Statistical Association*, 69(347):730–737, 1974.
- [69] Frank J. Massey Jr. The kolmogorov-smirnov test for goodness of fit. *Journal of the American Statistical Association*, 46(253):68–78, 1951.
- [70] George Marsaglia, Wai Wan Tsang, Jingbo Wang, et al. Evaluating kolmogorovs distribution. *Journal of Statistical Software*, 8(18):1–4, 2003.
- [71] Nikolai V Smirnov. On the estimation of the discrepancy between empirical curves of distribution for two independent samples. *Bull. Math. Univ. Moscou*, 2(2):3–14, 1939.
- [72] I T Young. Proof without prejudice: use of the kolmogorov-smirnov test for the analysis of histograms from flow systems and other sources. *Journal of Histochemistry & Cytochemistry*, 25(7):935–941, 1977. PMID: 894009.

- [73] Oracle Corporation. Fortran library reference: rand(). <https://docs.oracle.com/cd/E19957-01/805-4942/6j4m3r8vr/index.html>.
- [74] G. Gerbier M. Drees. Dark matter. Provided as a PDG review, 2011.
- [75] Luc Devroye. Sample-based non-uniform random variate generation. In *Proceedings of the 18th conference on Winter simulation*, pages 260–265. ACM, 1986.
- [76] Hilary Okagbue, Muminu Adamu, and Tim Anake. Closed form expression of the quantile function of maxwell-boltzmann distribution. *Advances and Applications in Statistics*, 54:179–197, 02 2019.
- [77] nojhan. Dreaming of metaheuristics. <http://nojhan.free.fr/metah/>, December 2007.
- [78] A. Blaauw, C. S. Gum, G. Westerhout, and J. L. Pawsey. The New I.A.U. System of Galactic Coordinates (1958 Revision). *Monthly Notices of the Royal Astronomical Society*, 121(2):123–131, 08 1960.
- [79] Craig J. Copi and Lawrence M. Krauss. Angular signatures for galactic halo weakly interacting massive particle scattering in direct detectors: Prospects and challenges. *Phys. Rev. D*, 63:043507, Jan 2001.
- [80] JD Vergados, Ch C Moustakidis, Yeuk-Kwan E Cheung, H Ejiri, Yeongduk Kim, and Jeong-Yeon Lee. Light wimp searches involving electron scattering. *Advances in High Energy Physics*, 2018, 2018.
- [81] J. L. Romeu and C. Grethlein. *A Practical Guide to Statistical Analysis of Material Property Data*. AMPTIAC, 2000.
- [82] Malcolm J Slakter. A comparison of the pearson chi-square and kolmogorov goodness-of-fit tests with respect to validity. *Journal of the American Statistical Association*, 60(311):854–858, 1965.
- [83] Taylor B Arnold and John W Emerson. Nonparametric goodness-of-fit tests for discrete null distributions. *R Journal*, 3(2), 2011.
- [84] Leo A. Goodman. Kolmogorov-smirnov tests for psychological research. *Psychological Bulletin*, 51, 1954.
- [85] DN McKinsey, D Akerib, S Bedikian, A Bernstein, A Bolozdynya, A Bradley, J Chapman, K Clark, T Classen, A Curioni, et al. The lux dark matter search. In *Journal of Physics: Conference Series*, volume 203, page 012026. IOP Publishing, 2010.
- [86] Teresa Marrodn Undagoitia and Ludwig Rauch. Dark matter direct-detection experiments. *J. Phys.*, G43(1):013001, 2016.
- [87] VN Lebedenko, HM Araújo, EJ Barnes, A Bewick, R Cashmore, V Chepel, A Currie, D Davidge, J Dawson, T Durkin, et al. Results from the first science run of the zeplin-iii dark matter search experiment. *Physical Review D*, 80(5):052010, 2009.

- [88] Craig E Aalseth, Phillip Spencer Barbeau, J Colaresi, JI Collar, J Diaz Leon, James E Fast, NE Fields, Todd W Hossbach, Andrea Knecht, Marek S Kos, et al. Cogent: A search for low-mass dark matter using p-type point contact germanium detectors. *Physical Review D*, 88(1):012002, 2013.

# Appendices

*Note* — Appendices are provided for completeness only and any content included in them will be disregarded for the purposes of assessment.

## .1 Further Kinematic Outputs

For completeness, I have included the simulated range of recoil angles,  $\phi$ , for a WIMP mass of  $100 \text{ GeV}/c^2$  to complement the figures provided previously. Below there are also the histograms showing the velocity distributions in each dimension, generated for the same data sample.

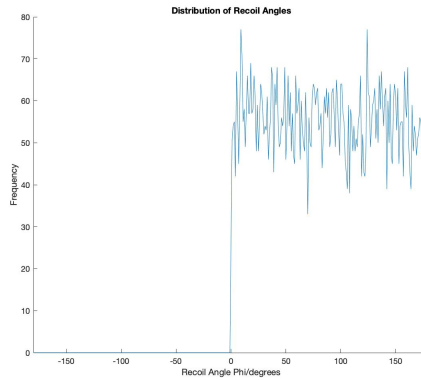


Figure 29. The recoil angles span a limited range, so that the momentum perpendicular to the initial motion of the WIMP remains constant.

## .2 Xenon Form Factor

The graph below shows the expected yield from Xenon when compared to select other elements. As a noble gas, it can be maintained at high purity, which allows for a great degree of sensitivity in measurement.

There is clearly benefit in choosing a variety of elements, and experiments such as ZEPLIN-II and -III had success with Argon (shown in blue above) [87], whilst novel approaches have been taken by the likes of the CoGeNT experiment using germanium crystals cooled to low temperature [88].

## .3 Instructions for implementing Form Factor in Simulation

The simulation at present stores a dataset with the form factor calculated for a range of energy values. In order to include this in the simulation, the following process may be

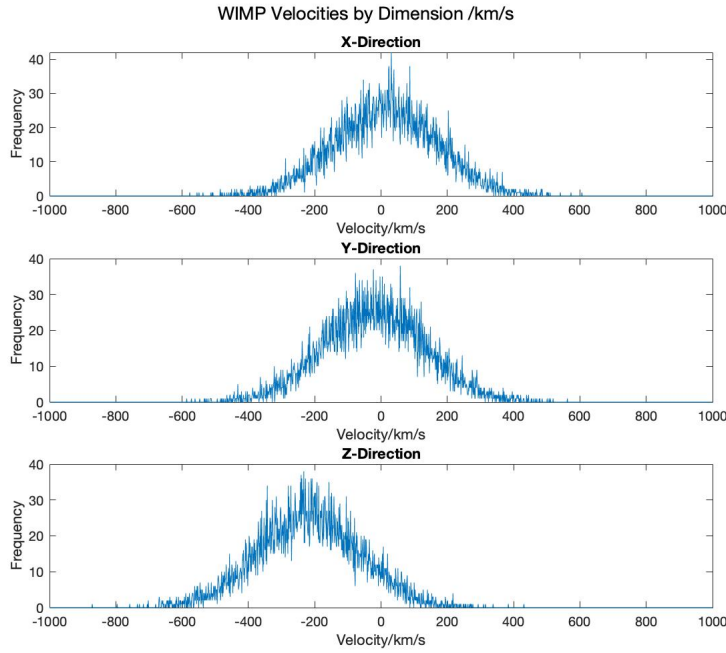


Figure 30. The simulated velocities with relation to each dimension.

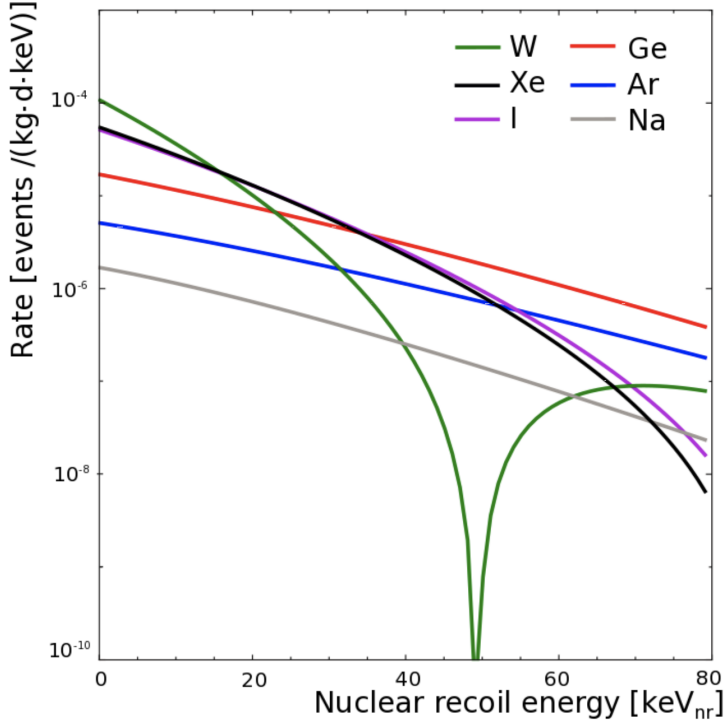


Figure 31. The differential yield for a range of target elements for direct detection considering 100 GeV/c<sup>2</sup> WIMP with a cross section of 1e-45 cm<sup>2</sup>, taken from [86]

added after the main sample loop and the binning of energy values is finished, but before the statistical analysis is carried out. This is not the most sophisticated option, but should provide a reasonable degree of accuracy. Looping over the energy values, simply multiply the histogram frequency for the recoil energy at each point by the corresponding form factor, ensuring this is applied to both the target and sample loops. This should modulate the distributions, which would easily be seen by viewing the energy spectra. It is not necessarily important to update the other kinematics in the experiment for consistency if the sole goal is to generate realistic recoil spectra, but this would be a good exercise to ensure that the results are physical and to be able to test the validity of the simulation.

There are more sophisticated ways to implement this in the experiment of course; I initially attempted to allocate the form factor values to the momentum transfer for each collision, and then assign each a probability of occurring that would modulate the frequency of interactions at each energy. Unfortunately I did not manage to implement this in time.

#### .4 Additional Statistical Outputs

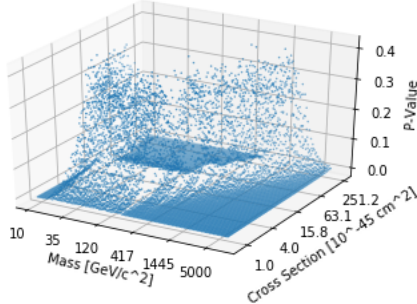


Figure 32. The 3-D representation of the Necib model p value data, target  $m_W = 100, \sigma = 9 \times 10^{-45} \text{cm}^2$

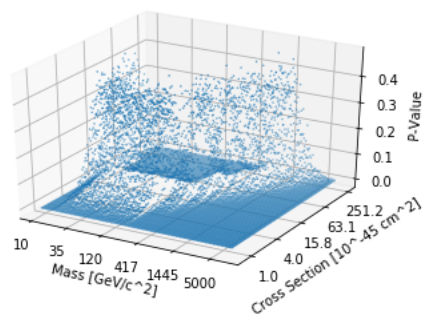


Figure 33. The 3-D representation of the Necib model p value data, target  $m_W = 60, \sigma = 4 \times 10^{-44} \text{cm}^2$